Fast ascent rate during the 2017–2018 Plinian eruption of Ambae (Aoba) volcano: a petrological investigation

Yves Moussallam, Estelle F. Rose-Koga, Kenneth T. Koga, Etienne Médard, Philipson Bani, Jean-Luc Devidal, Dan Tari

Fast ascent rate during the 2017-2018 Plinian eruption of Ambae (Aoba) volcano; a petrological investigation.

Yves Moussallam[1,2*], Estelle F. Rose-Koga[1*], Kenneth T. Koga[1*], Etienne Médard[1*], Philipson Bani[1], Jean-Luc Devidal[1], Dan Tari[3]

[1] *Université Clermont Auvergne, CNRS, IRD, OPGC, Laboratoire Magmas et Volcans, F-63000 Clermont-Ferrand, France*

[2] *Lamont-Doherty Earth Observatory, Columbia University, New York, USA*

[3] *Vanuatu Meteorology and Geohazards Department (VMGD), Vanuatu*

[*] *These authors have contributed equally to this work*

Corresponding author: Yves Moussallam; yves.moussallam@ird.fr

Keywords: volatile; melt inclusion; magma ascent; basaltic eruption; geo-speedometer

ABSTRACT

In September 2017, after more than a hundred years of quiescence, Ambae (Aoba), Vanuatu's largest volcano, entered a new phase of eruptive activity, triggering the evacuation of the island's 11,000 inhabitants resulting in the largest volcanic disaster in the country's history. Three subsequent eruptive phases in November 2017, March 2018 and July 2018 expelled some of the largest tropospheric and stratospheric SO_2 clouds observed in the last decade. Here, we investigate the mechanisms and dynamics of this eruption. We use major elements, trace elements, and volatiles in olivine and clinopyroxene hosted melt inclusions, embayments, crystals and matrix glasses together with clinopyroxene geobarometry and

olivine, plagioclase and clinopyroxene geothermometry to reconstruct the physical and chemical evolution of the magma as it ascends to the surface. Volatile elements in melt inclusions and geobarometry data suggest that the magma originated from depth of ~ 14 km before residing at shallow (~ 0.5 to 3 km) levels. Magma ascent to the surface was likely facilitated by shallow phreatic eruptions that opened a pathway for magma to ascend. Succeeding eruptive phases are characterised by increasingly primitive compositions with evidence of small amounts of mixing having taken place. Mg-Fe exchange diffusion modelling yields olivine residence times in the magma chamber ranging from a few days to a year prior to eruption. Diffusion modelling of volatiles along embayments (melt channels) from the first two phases of activity and microlite number density suggest rapid magma ascent in the range of 15 to 270 km/h, 4 to 75 m/s (decompression rates of 0.1 to ~2 MPa/s) corresponding to a short travel time between the top of the shallow reservoir and the surface of less than two minutes.

INTRODUCTION

Ambae (also known as Aoba; 167°50′E, 15°23′S), is an island volcano located in the central part of the Vanuatu archipelago. The volcano summit is located 3900 m above the sea floor and 1496 m above sea level (Fig. 1). The emerged part of the edifice is 38 × 16 km and host a pre- 2017 eruption population of about 11,000 inhabitants. Although part of a particularly active volcanic arc, Ambae's magmatic system has been very little studied compared to its volcanic neighbour Ambrym (e.g., Firth et al. 2016; Allard et al. 2016; Sheehan and Barclay 2016). Yet the volcano's magmatic activity together with the presence of large acid lakes at the volcano's summit, poses a particularly high risk to the island's population due to the potential for highly explosive phreato-magmatic eruptions and especially lahars. An understanding of Ambae's magmatic system is an essential first step towards a better

comprehension of its past and forecasting of its future activity. In this contribution, we aim to draw such an understanding by studying deposits from the 2017-2018 eruption of Ambae, the largest in recorded history.

Ambae is located in the central part of the Vanuatu arc, created by the north-eastward subduction of the Australian plate underneath the Pacific plate (e.g., Daniel et al. 1989). This central part of the arc is characterised by the collision of the D'Entrecasteaux ridge, a 100 km wide Eocene–Oligocene island arc complex on the Australian subducting plate, with the fore-arc (e.g., Collot et al. 1985). Ambae is a shield volcano composed of a pile of primitive basalts (Gorton 1977; Eggins 1993). At the summit is a 5 x 4 km caldera partially filled by 3 lakes one of which was considered among the world's largest acid crater lakes (Voui lake) (Bani et al. 2009a). According to local knowledge, the last significant eruption occurred about 350 years ago, with lava flows reaching the sea near N'dui N'dui (Warden 1970). Volcanic activity at Ambae in the last hundred years has been limited to fumarolic manifestation (Wiart 1995; Bani et al. 2009b). However since the early 1990s Ambae resumed eruptive activity within lake Voui, first with a phreatic eruption in 1995, followed by a Surtseyan eruption in 2005 that formed a 500 m width and 50 m high islet in the centre of the lake (Nemeth et al. 2006). This latter eruption has disrupted the equilibrium within lake Voui leading to a spectacular colour change from blue to red in 2006 (Bani et al. 2009b).

On 6 September 2017, a new eruptive period started with series of strong explosions (heard from neighbouring islands) that generated ash-laden plumes into the atmosphere. These first eruptions were likely phreatic, judging by the absence of juvenile material in the ejected products (Bani et al., in prep.), but injected large quantities (38,000 tons) of SO_2 into the atmosphere (OMI data, Bani et al., in prep.). On 22 September 2017, lava reached the surface

producing fire fountains, Strombolian eruptions and lava flows. In early October 2017 the surficial activity had subsided, the period from 22 September to 6 October 2017 is referred to here as phase 1 of activity. On 21 October 2017, a second phase of high-intensity eruptive activity started. Intense ash fall and acid rains were reported on coastal villages. 39,000 tons of SO_2 were injected on the first two days of activity alone (OMPS data, Bani et al., in prep.). By the end of November, the eruption intensity had subsided with ash and gas impacts limited only to the top of the island. The period from 21 October to 7 December 2017 is referred to here as phase 2 of activity. In mid-March 2018 a third intense eruptive phase started producing ash falls and acid rains with even more destructive impacts on the population and environment than during the prior phases. A night glow, presumably from fire fountains, could be seen from Maewo and Pantacost islands, 50 km away from the summit. Gas jetting was sustained for more than 20 days and clearly audible in a 15 km radius. The eruption intensity decreased around 15 April after significant release of volcanic gases to the atmosphere (123,000 tons released on April 6, 2018 alone; OMI data, Bani et al., in prep.). The period from mid-March to mid-April 2018 is referred to here as phase 3 of activity. Three months later, in mid-July 2018, the eruption intensity increased once again to its most violent and destructive eruptive period. Ash fall covered the entire island, momentarily plunging coastal villages in total darkness, causing houses to collapse. By early August 2018 the eruption intensity had waned. The period of July 2018 is referred to here as phase 4 of activity. This July 2018 episode released an estimated 400,000 tons of sulfur dioxide into the upper troposphere and stratosphere at an altitude of 16.9 km (NASA Earth Observatory, 2019). All together an estimated 3.2 Tg of SO_2 was released during the 2017-2018 Ambae eruption placing it among the top 6 largest eruption of the last 40 years in terms of SO_2 loading (Bani et al., in prep.). A detailed narrative of the eruption and its impacts in terms of ash fall, lahar and gas emissions will be presented elsewhere (Bani et al., in prep.).

In this contribution, we perform a petrological investigation of the magma expelled during the four phases of activity. We present major element, trace element, and volatile content in olivine and clinopyroxene hosted melt inclusions, embayments, matrix glasses and bulk rock together with clinopyroxene geobarometry, olivine, plagioclase, and clinopyroxene geothermometry and major element and volatile diffusion modelling. We find that the Ambae plumbing system extends from 0.5 to 14 km depth with most of the magma involved in the 2017-2018 eruption sourced from a shallow reservoir at 0.5 to 3 km depth. Phreatic eruptions in early September 2017 likely served as trigger to or facilitated the subsequent magmatic activity but was itself likely triggered by magmatic gases. Olivine residence times in the magma chamber(s) range from a few days to a year prior to eruption. We constrain the ascent rate of the magma from the shallow reservoir to the surface at 4 to 75 m/s. This fast ascent rate suggests that large amounts of pre-eruptive volatiles must have been present in the reservoir, consistent with satellite observations of large SO_2 emissions and of eruptive clouds reaching the lower stratosphere.

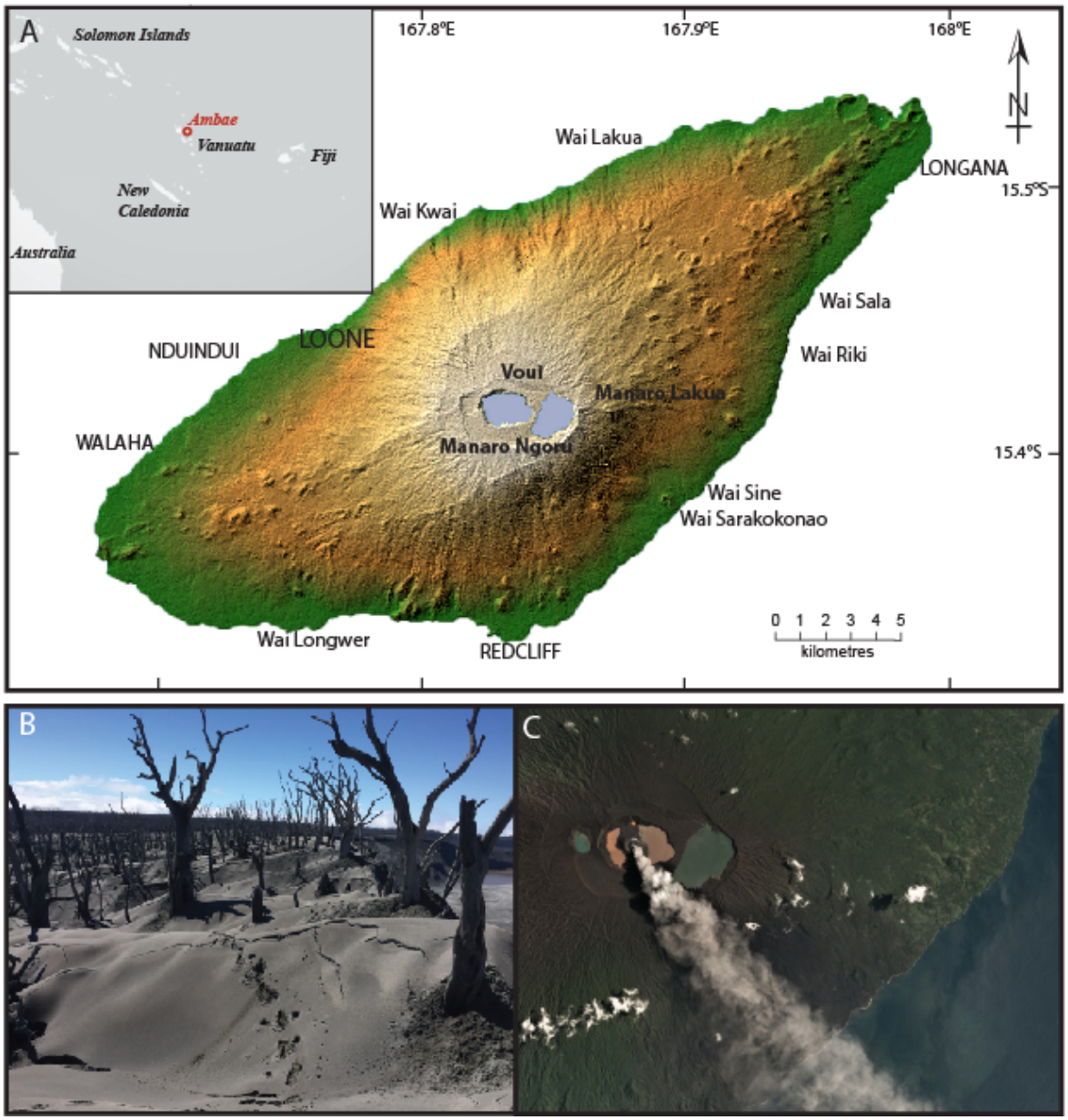

***Figure 1**: **A**. Topographic hill shaded Shuttle Radar Topography Mission (SRTM) image of Ambae island (credit NASA). Location of all coastal settlements are marked together with the location of Voui lake. Upper left inset shows the location of Ambae/Aoba island within the south Pacific. **B**. Ash deposit on the north-western part of Voui crater (image take on 21 May 2018). **C**. Planetscope Ortho tile satellite image of the summit area taken 10 March 2018 showing the strong degassing at that time (image credit: ESA)*

METHOD

Samples

Tephra samples from phase one (September 2017), two (November 2017) and three (March 2018) were collected in the summit area within a few days to weeks of deposition. Ash samples from phase four (July 2018) were collected 10 km west of the vent during deposition. Samples from phase 1, 2 and 3 consisted of lapilli-size scoria with fragments typically about 1 cm in diameter. Scoriae from eruptive phase 1, 2 and 3 and ash from eruptive phase 4 were embedded in epoxy resin and polished to investigate their texture and the composition of crystal phases and interstitial glasses. For eruptive phase 1, 2 and 3, part of the same samples was crushed and sieved, and melt-inclusion bearing, euhedral and unbroken olivine and pyroxene crystals were handpicked under a binocular microscope (in the 0.5- and 2-mm grain size fraction). Melt inclusions and embayments were exposed by polishing single crystals individually. Olivine crystals were oriented for polishing in order to expose a maximum length of the embayments, from the end to the mouth of the embayment. Polishing was performed without the use of diamond as to entirely avoid possible C contamination in subsequent ion probe analysis, instead silicon carbide mats for coarse polishing and corundum mats for final 3 µm, 1 µm and ¼ µm polishing were used. Single crystals were subsequently mounted in indium. Melt inclusions are entirely glassy, often contain a contraction bubble and are typically about 50 to 200 µm in diameter (Fig. 2B).

Analyses of major elements

Bulk tephra samples were powdered, mixed with $LiBO_2$, and melted in an induction oven at 1050 °C for 4.5 min using graphite crucibles. Resulting glass beads were then dissolved in a solution of deionized water and nitric acid and finally diluted by a factor of 2000. The

149 solutions were analysed by ICP-AES at Laboratoire Magmas et Volcans in Clermont-
150 Ferrand.
151 Individual melt inclusions, embayments, matrix glasses and crystals were analysed with a
152 Cameca SX100 electron microprobe at the Laboratoire Magmas et Volcans in Clermont-
153 Ferrand. For crystalline phases, beam conditions of 15 kV and 15 nA were employed,
154 while for glass analyses, the beam current was 6-8 nA and the beam defocussed to 10 µm.
155 Sodium was analysed first as to limit the effects of Na loss. The instrument was calibrated on
156 natural and synthetic mineral standards and glasses : wollastonite (Si, Ca), $MnTiO_3$ (Ti, Mn),
157 Al_2O_3 (Al in minerals), standard glass VG2 (Al in glasses, see Óladóttir et al. 2008), Cr_2O_3
158 (Cr), fayalite (Fe), forsterite (Mg), NiO (Ni), albite (Na), orthoclase (K) and apatite (P).
159 Counting times were 10s minimum. Olivine core to rim transects were acquired by making
160 measurements every 10 µm from the crystal centre to the rim along a line perpendicular to
161 the crystal face. In order to produce accurate analyses for minor elements, acceleration
162 voltage was increased to 20 kV, beam current to 100 nA, and counting times to 20 s (Fe), 50 s
163 (Mn, Ni), and 100 s (Al, P).
164
165 **Ion Probe analyses of volatile elements**
166 Volatile (H_2O, CO_2, Cl, F, S) content in melt inclusions, embayments, and matrix glasses
167 were determined using a Cameca IMS 1280 ion microprobe at CRPG-CNRS-Nancy.
168 Analytical conditions were similar to other volatile studies (e.g., Hauri et al. 2002; Bouvier et
169 al. 2008; Shimizu et al. 2009; Rose-Koga et al. 2014; Moussallam et al. 2015). We used a Cs^+
170 primary beam with a current of 1 nA and an electron gun to compensate for charge build-up
171 at the sample surface. A 3-minute pre-sputter with a 30 × 30 µm square raster was applied,
172 then analyses were performed on the 15 to 20 µm spot in the center of the rastered-clean area
173 by a mechanical aperture placed at the secondary ion image plane. The mass resolving ≈7000

(with the contrast aperture at 400 µm, the energy aperture at 40 eV, the entrance slit at 52 µm and the exit slit at 173 µm) meant that complete discrimination of mass interferences was achieved ($^{34}S^{1}H$ on ^{35}Cl, ^{17}O on $^{16}O^{1}H$, $^{29}Si^{1}H$ on ^{30}Si and $^{31}P^{1}H$ on ^{32}S). We collected signals for ^{12}C (8 seconds), ^{17}O (3 seconds), $^{16}O^{1}H$ (6 seconds), ^{18}O (3 seconds), ^{19}F (4 seconds), ^{27}Al (3 seconds), ^{30}Si (3 seconds), ^{32}S (4 seconds) and ^{35}Cl (6 seconds; counting times in parenthesis), with 2 seconds waiting time after each switch of the magnet. This cycle was repeated 10 times during one analysis. One measurement lasted 12 min per spot.

The concentrations were determined using calibration curves (see supplementary materials) obtained, at the beginning and at the end of each session, by measuring a set of natural basaltic glasses during the same session and under the same analytical conditions (KL2G, Jochum et al. 2006); KE12, Mosbah et al. 1991; VG2, Jarosewich et al. 1980; experimental glasses N72, M35, M40 and M48, Shishkina et al. 2010 and MacQuarie glasses 47963 and 25603, Kamenetsky et al. 2000) with a large range of concentrations of volatile elements overlapping those of our samples. Maximum errors, based on reproducibility over 10 cycles of analyses, were less than 15% for CO_2, 3% for Cl, 4% for S, and 5% for F and H_2O.

LA-ICP-MS analyses of trace elements

Trace element measurements on melt inclusions, embayments and glasses were carried out using a laser ablation system (193 nm Excimer Resonetics M-50E) associated with an inductively coupled plasma mass spectrometer (Agilent 7500 cs LA-ICPMS at the Laboratoire Magmas et Volcans, Clermont-Ferrand). Analysis were performed following classical procedures outlined in previous studies (e.g., Le Voyer et al. 2010; Rose-Koga et al. 2012). We used a pulse energy of about 3 mJ, a spot diameter between 15 and 33 µm and a laser pulse frequency of 2-3Hz, depending in the inclusion size to keep a fluence at sample surface of about 4 J/cm^{-2}. The background was measured for 30 to 40 seconds before ablation

199 and analysis time was approximately 100s. Data reduction was performed using the
200 GLITTER software (www.es.mq.edu.au/GEMOC). This technique uses CaO (measured by
201 EMP) as an internal standard. Reproducibility and accuracy of the analysis were constrained
202 by systematic analysis of 2 standards BCR2-G and 612 at the beginning, in the middle and at
203 the end of the session. Typical errors on the samples (1σ error of mean) is less than 10 % for
204 all trace elements, except for Lu (<20%) and B (<40%).
205
206 **Volatile diffusion modelling**
207 Concentration profiles recorded in the embayments were fitted by a diffusion model similar
208 to that of Ferguson et al. (2016). While the detail of the model and test results are explained
209 in the Supplementary, a brief description is given here. An embayment profile was measured
210 in a tube-like pocket of melt found within an olivine crystal. Because of its shape and
211 incompatibility of volatile elements, such as H, C, S, Cl, and F, in olivine, diffusive exchange
212 of elements was considered only possible at the mouth of the embayment. This justifies the
213 use of diffusion solution in 1-D geometry. Naturally, the concentrations of volatile elements
214 are systematically lower at the mouth of embayment. Having these geometrical constraints,
215 we have developed a model with the following initial and boundary conditions for Fick's
216 Second Law:

217 $$\frac{\mathrm{d}C}{\mathrm{d}t} = D(C_W)\frac{\partial^2 C}{\partial x^2}, \qquad (1)$$

218 $$C = c_{initial}, x > 0, t = 0; \;\; C = \; c_{initial}, x = \infty, t > 0,$$

219 $$C = f(t), x = 0,$$

220 where $D(C_W)$ is the diffusion coefficient of water in melt as a function of total dissolved
221 water concentration; C, the concentration of diffusing species; t, time; and x, distance.
222 Concentrations of volatile elements were set at a constant value $c_{initial}$, in the embayment,
223 determined by the plateau concentration value inside the embayment. Concentration at the

interface was set by a function with respect to time, which determines H_2O-CO_2 solubility in magma along the linear isothermal decompression. In a magma ascending for eruption, and for fast diffusing species such as H_2O, a closed system degassing approximates the volatile element segregation better than an open system, as the latter requires complete segregation of magma from gas at every instant of degassing. We used SolEx (Witham et al. 2012) to determine the closed system, equilibrium degassing path for H_2O, CO_2, S, and Cl, and the f(t) was determined from the SolEx result with a constant decompression rate (dP/dt). The diffusion equation was solved by Crank-Nicolson finite difference method for the 1-D geometry.

This diffusion calculation had therefore four parameters: (1) diffusion coefficient, (2) initial concentration, (3) concentration of a volatile element at x=0 which changes with time (*i.e.* decompression), (4) the mass of equilibrium bubble/fluid present at the moment of the magma ascent, and (5) the decompression rate. The first three parameters were independently determined with reasonable confidence from the experimental data, concentration profile, and magma temperature. The parameter (4) was unknowable, and it influenced the degassing path significantly (see the Supplementary). Here, we have tested its influence by varying from 0 to 1 wt % of pre-ascent volatile mass. By setting four parameters, the decompression rate was determined by minimizing the least-square residuals. While the method of Ferguson et al. (2016) minimizes X simultaneously for three volatile species (H_2O, CO_2, and S), it was not possible in our case. Diffusion profile of each volatile species were hence solved separately. R-based script, together with an example profile is given in Appendix B.

Olivine diffusion modelling

Chemical gradients (Fe–Mg) in olivines were modelled in one dimension with the DIPRA software program (Girona and Costa 2013). DIPRA is a finite difference code that solves Fick's second law of diffusion in order to model the one-dimensional diffusion of Fe – Mg (as forsterite, Fo = Mg/(Mg + Fe), in mole fraction), Mn, Ni, and Ca in olivine. Diffusion anisotropy was accounted for by determining the olivine crystallographic axes using EBSD and the angles between the electron microprobe traverse and the three crystallographic axes. Temperature and pressure calculations are detailed below, oxygen fugacity was fixed at the Nickel-Nickel-Oxide buffer in all calculations. Initial conditions for sample Ph1Ol2E_P1 and Ph1Ol2E_P2 used a step function while all other calculations were performed using a homogeneous profile (see Fig. S6). The use of a step function for Ph1Ol2E_P1 and Ph1Ol2E_P2 was justified by the high and non-random residual that would result from using a homogeneous profile. Note that the effect of water on the Fe-Mg interdiffusion (e.g., Wang et al. 2004; Hier□Majumder et al. 2005) is not taken into consideration in the DIPRA calculations.

Post-entrapment crystallisation modelling

Corrections of major and trace element composition in olivine-hosted melt inclusions for post entrapment crystallisations (PEC) was performed. It consisted of dissolving increments of equilibrium olivine into the melt inclusion liquid until the Fe-Mg Kd reaches the equilibrium value. The equilibrium value for the Mg/Fe exchange coefficient between olivine and liquid, Kd, was determined by a model accounting for the influence H_2O and alkalies (Toplis 2005 with T = 1145 ºC and P = 1000 bars), and the predicted Kd = 0.25±0.01. It should be noted that this value of Kd lower than the common value of 0.3 reflects that the Ambae melts were rich in Na_2O and K_2O. To test the effect of oxygen fugacity, Fe^{3+}/Fe_{tot} ratio was varied from 0.14 to 0.32 for the PEC calculation, reflecting the range observed for subduction zone

magmas, from FMQ-1 to FMQ+2; (e.g., Kress and Carmichael 1991; Bénard et al. 2018). With Fe^{3+}/Fe_{tot} = 0.14, we added successive increment of olivine back into the melt recalculating an observed Kd after each step and the process stopped when observed Kd = predicted Kd (0.25±0.01 here). By doing this, the mean mass of olivine added was only of 1% (with a standard deviation of 0.2%, n=57) suggesting that very little PEC took place. At higher Fe^{3+}/Fe_{tot} =0.32 (FMQ+2) or Fe^{3+}/Fe_{tot} =0.23 (FMQ+1), the redox-corrected observed Kd is already too high compared to the "Toplis-predicted" Kd so that no olivine can be added to the melt. In the following, the corrected value reported are calculated for Fe^{3+}/Fe_{tot} = 0.14.

Estimation of microlite number density

Toramaru et al. (2008) developed a model to link microlite number density (N) in pyroclastic rocks to the rate of water exsolution which in turn can be linked to the rate of magma ascent. Microlite crystallization can happen as a consequence of cooling or decompression-induced degassing. In the case of decompression-induced degassing, a numerical simulation performed by Toramaru (2008) shows that the microlite number density is directly linked to the increase in liquidus temperature caused by degassing:

$$\frac{\partial T_L}{\partial t} = \left(\frac{N}{a}\right)^{2/3} \qquad (2)$$

With the constant *a* mostly a function of melt chemistry and water concentration:

$$a = 3.10^{15+0.345\left(C_{SiO_2}-50\right)-0.65C_{H_2O}} \qquad (3)$$

where major element concentrations are in weight %.

The relationship between the increase in liquidus temperature T_L and the degassing rate is given by the derivative of the liquidus depression curve:

$$\frac{\partial T_L}{\partial t} = \frac{\partial T_L}{\partial C_{H_2O}} . \frac{\partial C_{H_2O}}{\partial t} \qquad (4)$$

296 The liquidus depression curve has been determined experimentally for olivine ($\frac{\partial T_L}{\partial C_{H_2O}} =$

297 $40.4 - 5.94C_{H_2O} + 0.2283C_{H_2O}^2$; Médard and Grove 2008), and plagioclase ($\frac{\partial T_L}{\partial C_{H_2O}} =$

298 $54.66e^{-0.29C_{H_2O}}$; Almeev et al. 2012) in basaltic melts. In the absence of an experimental

299 calibration for clinopyroxene, we calculated ($\frac{\partial T_L}{\partial C_{H_2O}} \sim 26$) for the bulk scoria of phase 1 using

300 the pMelts software (Ghiorso et al. 2002).

301 The degassing can in turn be converted into a decompression rate using the derivative of the

302 water solubility curve:

303 $$\frac{\partial P_{H_2O}}{\partial t} = \frac{\partial P_{H_2O}}{\partial C_{H_2O}} . \frac{\partial C_{H_2O}}{\partial t} \qquad (5)$$

304 For our trachybasaltic bulk composition, we fit a quadratic function to the solubility data

305 produced by the model of Moore et al. (1998) which gives $\frac{\partial P_{H_2O}}{\partial C_{H_2O}} = 182.3C_{H_2O}$

306 In a steady state, the decompression rate at the microlite nucleation depth is linked to the

307 ascent velocity (Toramaru et al. 2008):

308 $$V_N = \frac{1}{\rho g} . \frac{\partial P_{H_2O}}{\partial t} \qquad (6)$$

309 where ρ is the magma density at the microlite nucleation depth.

310

311 # RESULTS

312 **Mineralogy**

313 The investigated scoriae are glassy, and typically have low crystallinity (Fig. 2A), with rare

314 phenocrysts of plagioclase, olivine, and clinopyroxene, and microlites of the same phases.

315 Small euhedral spinel microlites are also present, often associated with olivine phenocrysts

316 (Fig. 2B). Most olivine phenocrysts have compositions ranging from Fo_{85} to Fo_{79}, as expected

317 for equilibrium with the bulk rock compositions (Table S1, S2, S3, S4, Fig. 3 and 4). Four

318 types of zoning patterns can be identified in olivine phenocrysts (Fig. 3, 4B): (1) no zoning

(homogeneous crystals, Fig 3D, 4B); (2) normal zoning (Fig 3A, 3B, , 3C, 3F, 3G 4B); (3) reverse zoning (Fig 2B, 2F, 3H, 3I); and (4) complex zoning (Fig 2E). Homogeneous crystals are dominant in phase 1, and a few are still present in phase 2. Crystals with weak normal zoning (less than 1.5 Fo unit) are only present in phase 1 and again in phase 4. Reverse zoning is typical for most crystals from phase 2 and 3. Crystals with the stronger reverse zoning also show rounded edges indicative of dissolution. Reverse zoning can be interpreted as reflecting either magma mixing (Ruth et al. 2018) or reheating of a magma reservoir. Complex zoned phenocrysts have a weak internal reverse zoning very similar to the one observed in the previous type, followed by a strong normal zoning. These complex zoned phenocrysts are associated with a high microlite density, and present mostly in phase 1, although one crystal has been found in phase 2 and one in phase 3. These complex zoned phenocrysts are very similar to the olivine phenocrysts described from the April 2007 eruption of Piton de la Fournaise (Reunion Island) where they have been interpreted as products of lateral magma transfer in the plumbing system (Albert et al. 2019). As for the Reunion samples, normal zoning patterns around melt inclusions are identical to normal zoning patterns near the crystal rims, indicating that the zoning is not due to magma mixing (Albert et al. 2019).

A significant fraction of the olivine phenocrysts (Fig. 4A) have core compositions more magnesian than Fo_{84} and are thus not in equilibrium with any of the measured bulk rock compositions (Fig. 4). We interpret those crystals as antecrysts, formed from a batch of more primitive magma. A few small olivine microlites have compositions ranging from Fo_{82} to Fo_{74} (Table S3). Clinopyroxene phenocrysts are normally zoned, with Mg# ranging from 85 to 78 (Table S5, calculated assuming all Fe as FeO). Oscillatory zoning is occasionally observed (Fig. 2D). Clinopyroxene microlites are small and difficult to analyse but have Mg# in the range 80-72. Plagioclase phenocrysts are euhedral, normally zoned and commonly

show oscillatory zoning (Fig.2C). Their composition varies from An_{81} in the core to An_{70} near the rims (Table S6). Euhedral plagioclase microlites have compositions varying from An_{80} to An_{58}. Spinel compositions are highly variable: spinel included in olivine phenocrysts are chromites (41 wt% Cr_2O_3), whereas the rare spinel microlites tend to be richer in iron (58 wt% $FeO+Fe_2O_3$ on average, up to 76 wt%).

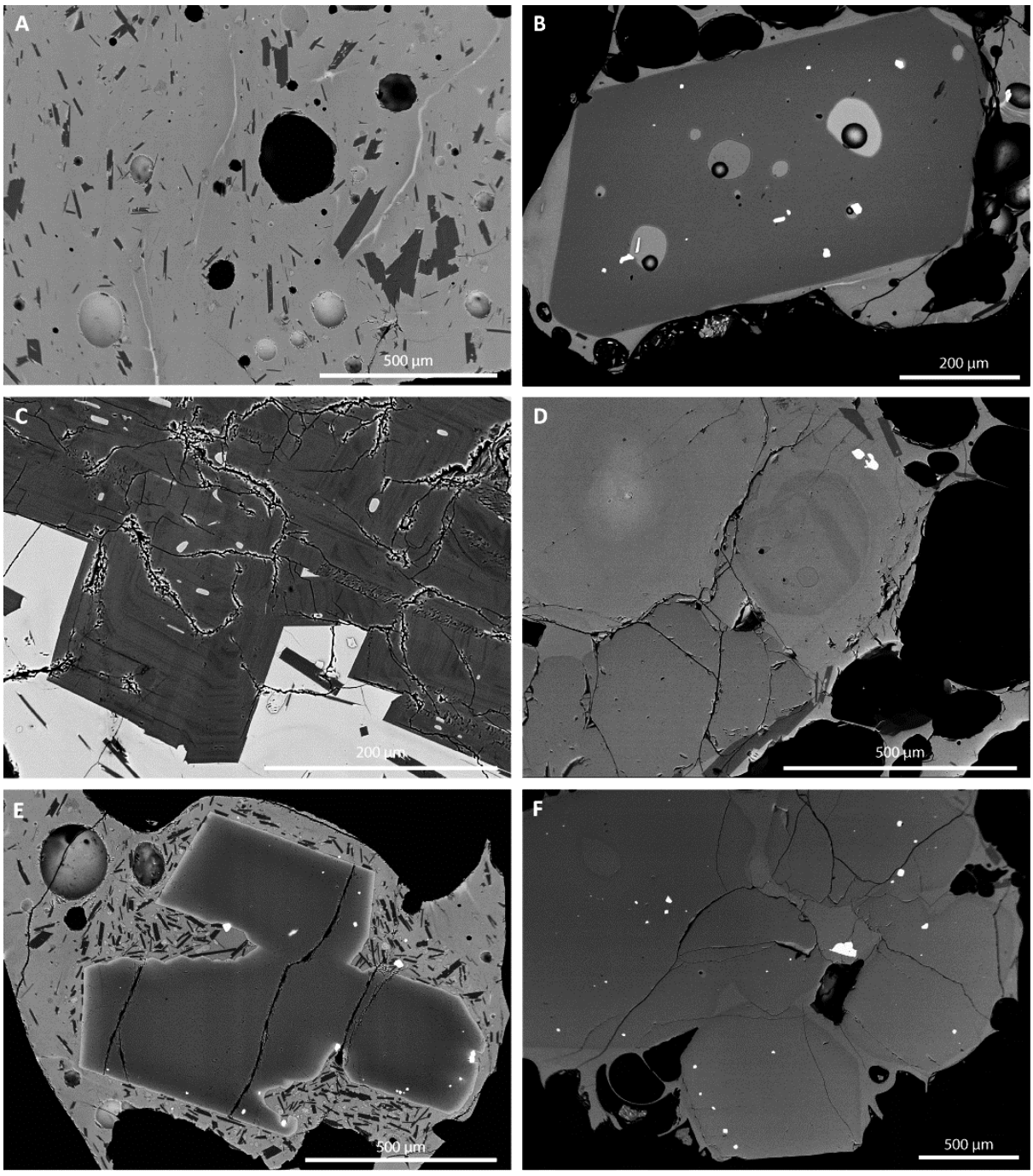

Figure 2: A. *BSE microphotograph of the typical glassy texture of the pyroclasts (phase 1), with plagioclase (micro-)phenocrysts and microlites and a few olivine and clinopyroxene microlites.* ***B****. BSE microphotograph of a normally zoned olivine phenocryst with large glassy melt inclusions associated with spinel crystals and retraction bubbles (phase 2).* ***C****. Enhanced BSE microphotograph of oscillatory zoning in a plagioclase phenocryst that contain small melt-inclusions (phase 1).* ***D****. BSE microphotograph of clinopyroxene phenocrysts with complex oscillatory zoning and melt inclusions (phase 2). E. BSE microphotograph of an olivine phenocryst showing complex zoning: slight inverse zoning around the core, followed by clean normal zoning on the edges (phase 1). The phenocryst also contains spinel inclusions and is surrounded by an increased microlite density. F. Enhanced BSE microphotograph of a group of olivine phenocrysts with a slight reverse zoning around the edges (phase 2). The phenocrysts contain spinel and melt inclusions.*

***Figure 3**: Rim to core electron microprobe %Fo (mol%) (= 100 × Mg/ [Fe + Mg]), Ca, Mn, and Ni traverses in olivine crystals from phase 1 (**A to E**) and phase 3 (**F to J**). AO10, AO11, AO22 and AO18 show predominantly normal zoning with AO10 showing an alternation from normal to reverse zoning close to the rim. AO12 shows no resolvable zoning pattern. Ol5ph3, Ol2ph3 and Ol1ph3 show normal zoning while Ol7ph3 and Ol3ph3 shows reverse zoning.*

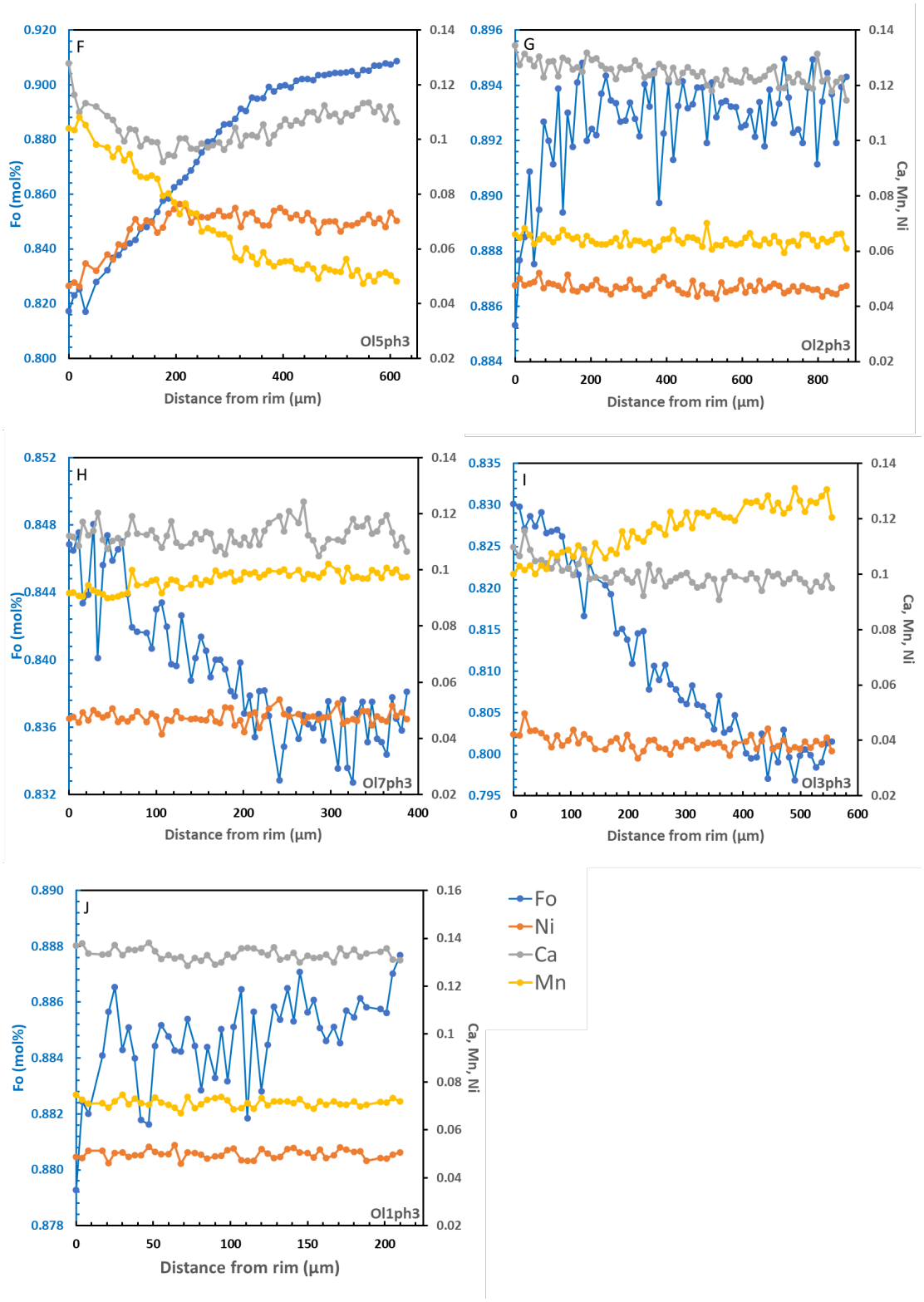

Figure 3con: *Rim to core electron microprobe %Fo (mol%) (= 100 × Mg/ [Fe + Mg]), Ca, Mn, and Ni traverses in olivine crystals from phase 1 (**A to E**) and phase 3 (**F to J**). AO10, AO11, AO22 and AO18 show predominantly normal zoning with AO10 showing an alternation from normal to reverse zoning close to the rim. AO12 shows no resolvable zoning pattern. Ol5ph3, Ol2ph3 and Ol1ph3 show normal zoning while Ol7ph3 and Ol3ph3 shows reverse zoning.*

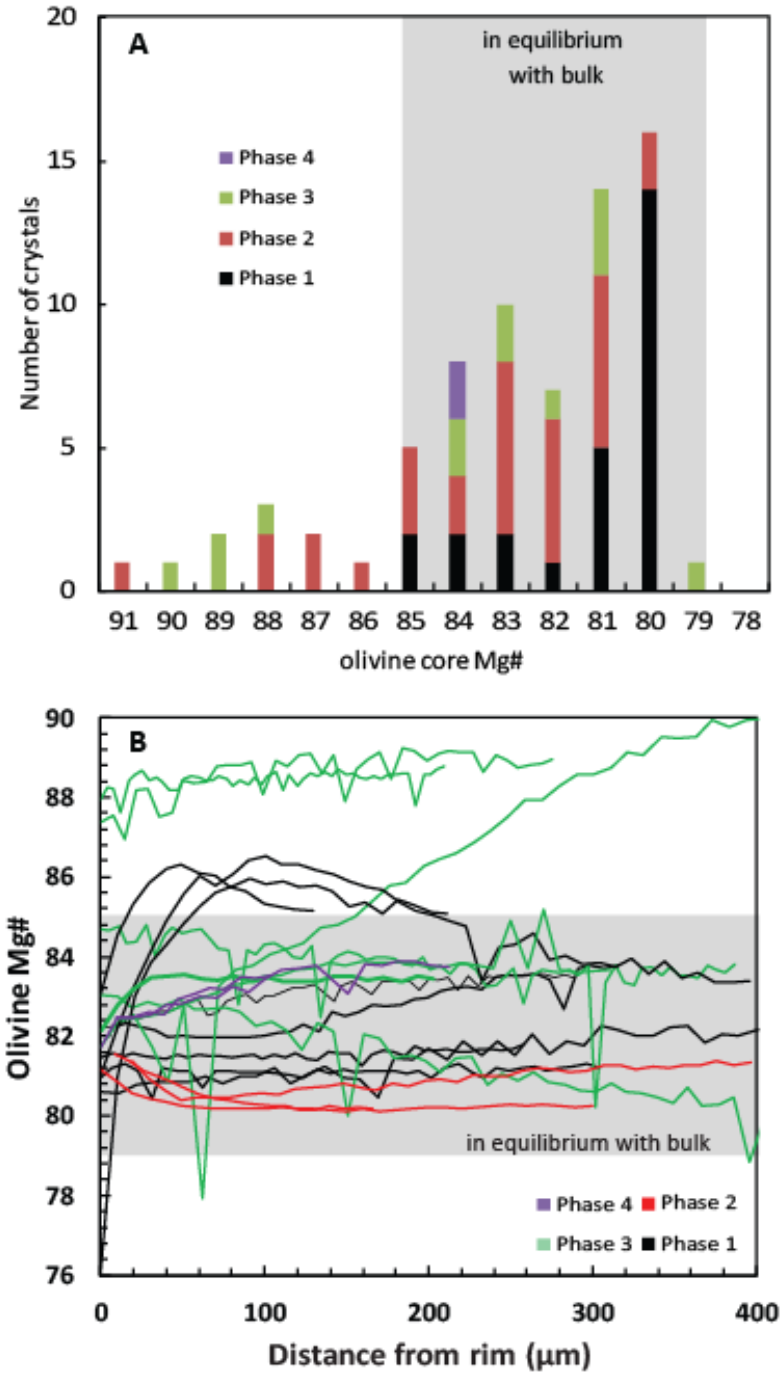

376

377 ***Figure 4****: A. Frequency diagram of the Fo content in olivine cores from phase one, two and*
378 *three. The range of Fo composition in equilibrium with bulk is calculated using measured*
379 *bulk rock compositions and a Kd of 0.3. Note that a significant fraction of phase 2 and 3*
380 *olivines have core composition more magnesian-rich than expected for equilibrium with the*
381 *bulk. B. Fo profiles of olivine phenocrysts from phases 1,2,3 and 4.*

382

383 **Major elements**

384 The PEC corrected composition of melt inclusions, embayments and matrix glasses in major
385 and trace element is given in Tables S1 and S7. Uncorrected compositions are given in Tables
386 S2 and S8.

387

388 Samples for the 2017-2018 eruption are the most differentiated volcanic rocks on the island,
389 with the exception of one trachyandesite analysis reported by Eggins (1993). The bulk rock
390 compositions (Table S1) plot in the trachybasalt and basaltic trachyandesite fields of the TAS
391 diagram (Fig. 5), as an extension of previously published analyses for Ambae island (Warden
392 1970; Gorton 1977; Eggins 1993). Previously reported whole rocks (and melt inclusion)
393 compositions from older (undated) deposits on Ambae are more primitive, mostly tholeiitic
394 and alkali basalts. The younger rocks of Ambae belong to the low-Ti suite of Eggins (1993).
395 This suite starts with voluminous magnesian olivine- and clinopyroxene-phyric basalts
396 ("ankaramites") that form the largest part of the island. More differentiated plagioclase-
397 phyric basalts are confined to stream courses and represent the youngest eruptive products of
398 the volcano, including lava flows from the latest significant eruption of the volcano that
399 produced the N'dui N'dui flow about 350 years ago (Warden 1970). Products of the 2017-
400 2018 eruptive phase are slightly more differentiated than these plagioclase-phyric basalts, and
401 likely represent further evolution along a fractional crystallization trend (Fig. 5). In total
402 alkali-silica space, most inclusions plot as alkali basalt, trachy-basalt or basaltic trachy-
403 andesite while matrix glasses are basaltic trachy-andesite in composition. In details, melt
404 inclusions, matrix glasses and bulk rock compositions from phase 1 tend to be slightly more
405 evolved than the ones of phase 2, 3 and 4.

406

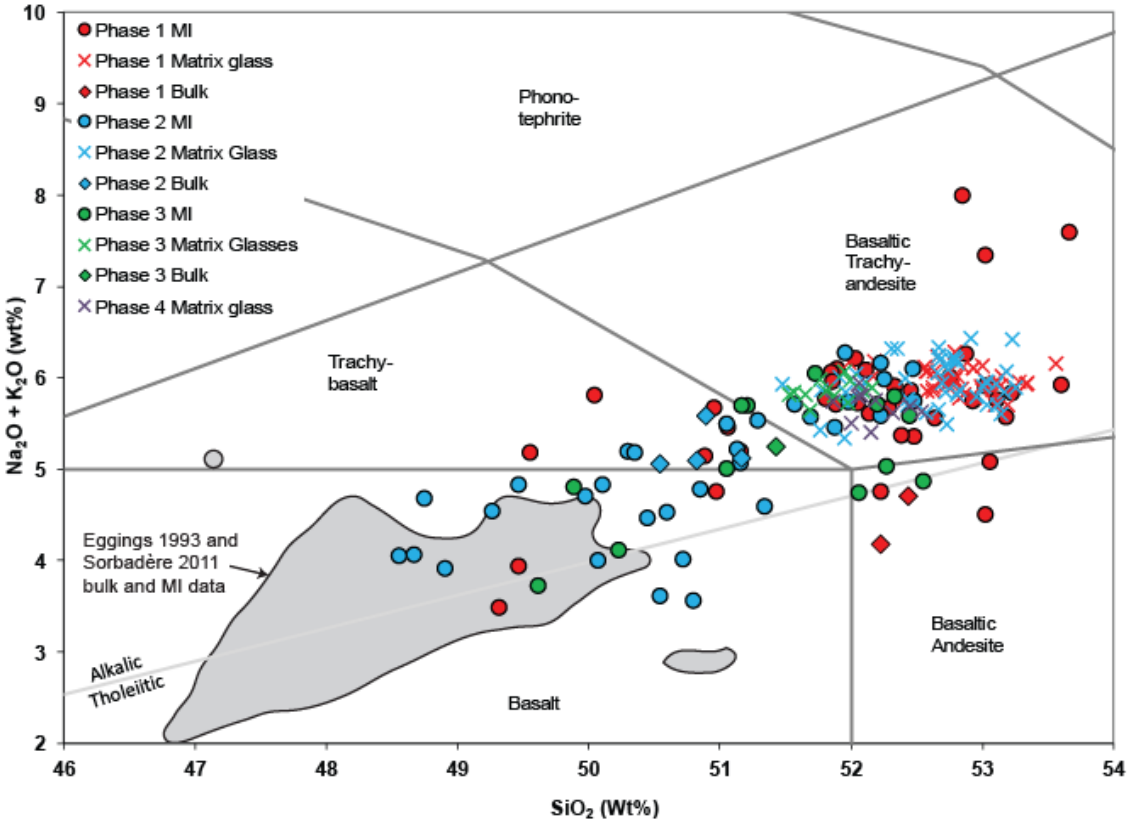

Figure 5*: Total alkalis versus silica. Melt inclusions, matrix glasses and bulk rock compositions (all normalized) are reported for the first three phases of eruptive activity between 2017 and 2018 and matrix glass compositions are reported for phase 4. Bulk rock and melt inclusion composition data from older (undated) deposits are from Eggins (1993) and Sorbadere et al. (2011).*

Melt inclusions have Mg# ranging from 31.7 to 59.6 (assuming all iron is FeO). Host olivine crystals have compositions ranging from Fo_{79} to Fo_{91}. As expected for near equilibrium melt inclusion-host pairs, there is a clear correlation between the olivine and melt inclusions compositions (Fig. 6A). Interestingly, olivine erupted during the first phase of activity (September 2017) tend to have lower Forsterite content (Fo < 84%) and to contain inclusions with low Mg# (Mg# < 50) while olivine erupted during the subsequent two phases of activity (November 2017 and March 2018) have a larger range of Forsterite content (Fo up to 91%) and contain inclusions with a larger range of Mg# (Mg# up to 60). In addition, melt inclusions from the first phase tend to be richer in Si, Al, Fe, Mn and K, and poorer in Ca and Mg compared to melt inclusions from the second and third phases (Fig. 6). This is also seen

424 with the interstitial glasses which show a small increase in MgO, Mg# and CaO/Al_2O_3, and a
425 small decrease in Na_2O and K_2O between phases 1, 2, 3 and 4.
426

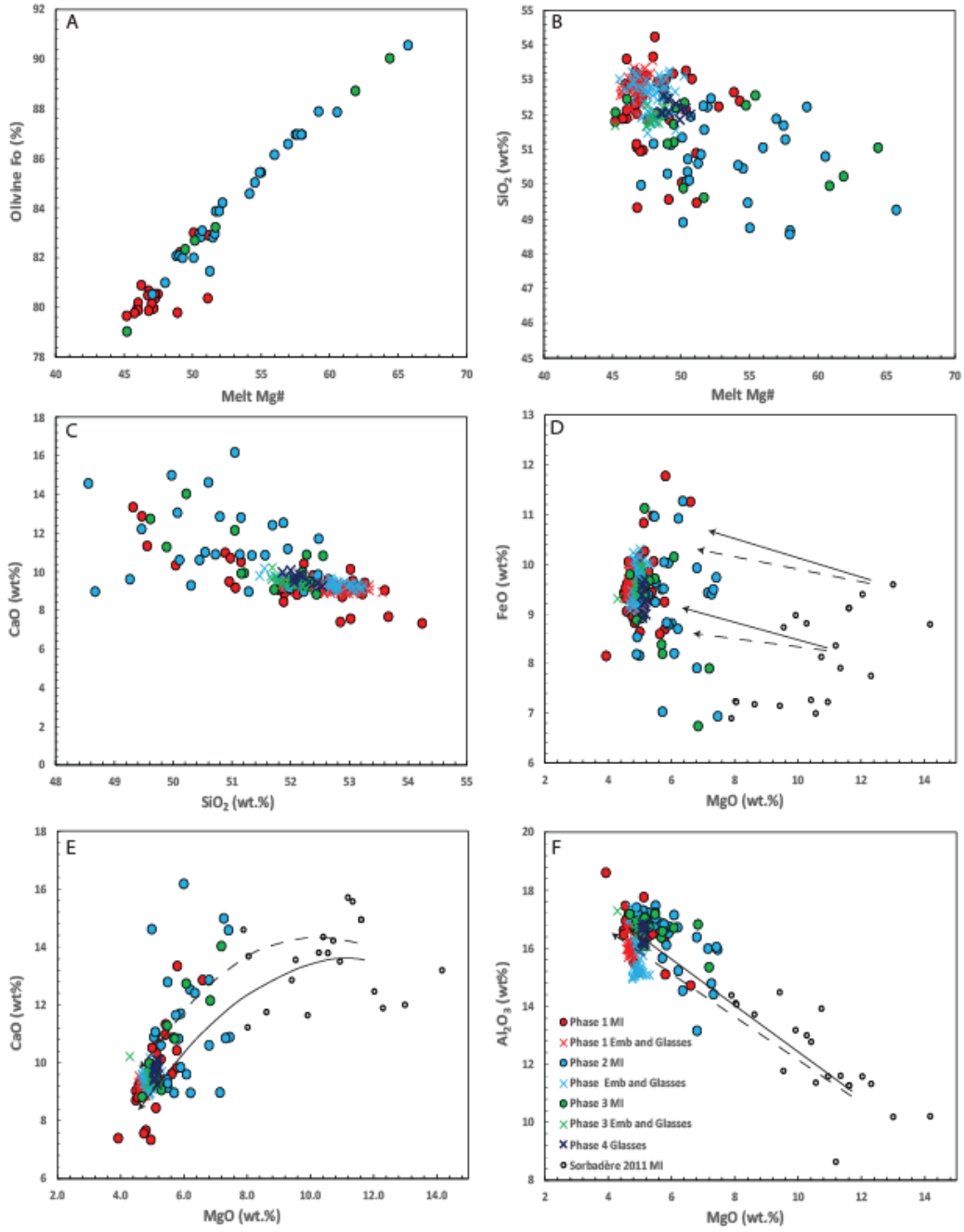

427

428 ***Figure 6****: Major element compositions of olivine and pyroxene-hosted melt inclusions*
429 *(olivine-hosted inclusions are PEC-corrected).* ***A****. Olivine Forsterite content vs melt inclusion*
430 *Mg#.* ***B****.* SiO_2 *vs melt Mg#.* ***C****.* CaO *vs* SiO_2*.* ***D****.* FeO_t *vs MgO.* ***E****.* CaO *vs MgO.* ***F****.* Al_2O_3 *vs*
431 *MgO. More primitive melt inclusions data from Ambae are also shown, together with*
432 *MELTS-calculated liquid lines of descent at 200 MPa (dotted arrow) and 500 MPa (solid*
433 *arrow)* (Sorbadere et al. 2011).
434

435 **Trace elements**

436 Trace and rare earth elements concentrations in melt inclusions and matrix glasses show no
437 systematic differences between the first three eruptive phases (Fig. S4 and 7). The rare earth
438 element distribution, normalised to chondrite (Sun and McDonough 1989), is typical of arc
439 magmas, being depleted in heavy rare earth elements. The positive correlations, passing close
440 to the origin, between incompatible element pairs (Fig. 7A and 7B) show that melt inclusion
441 compositions of the three eruption phases plot on a single trend of magma differentiation,
442 suggesting they belong to a co-genetic magmatic series.

443

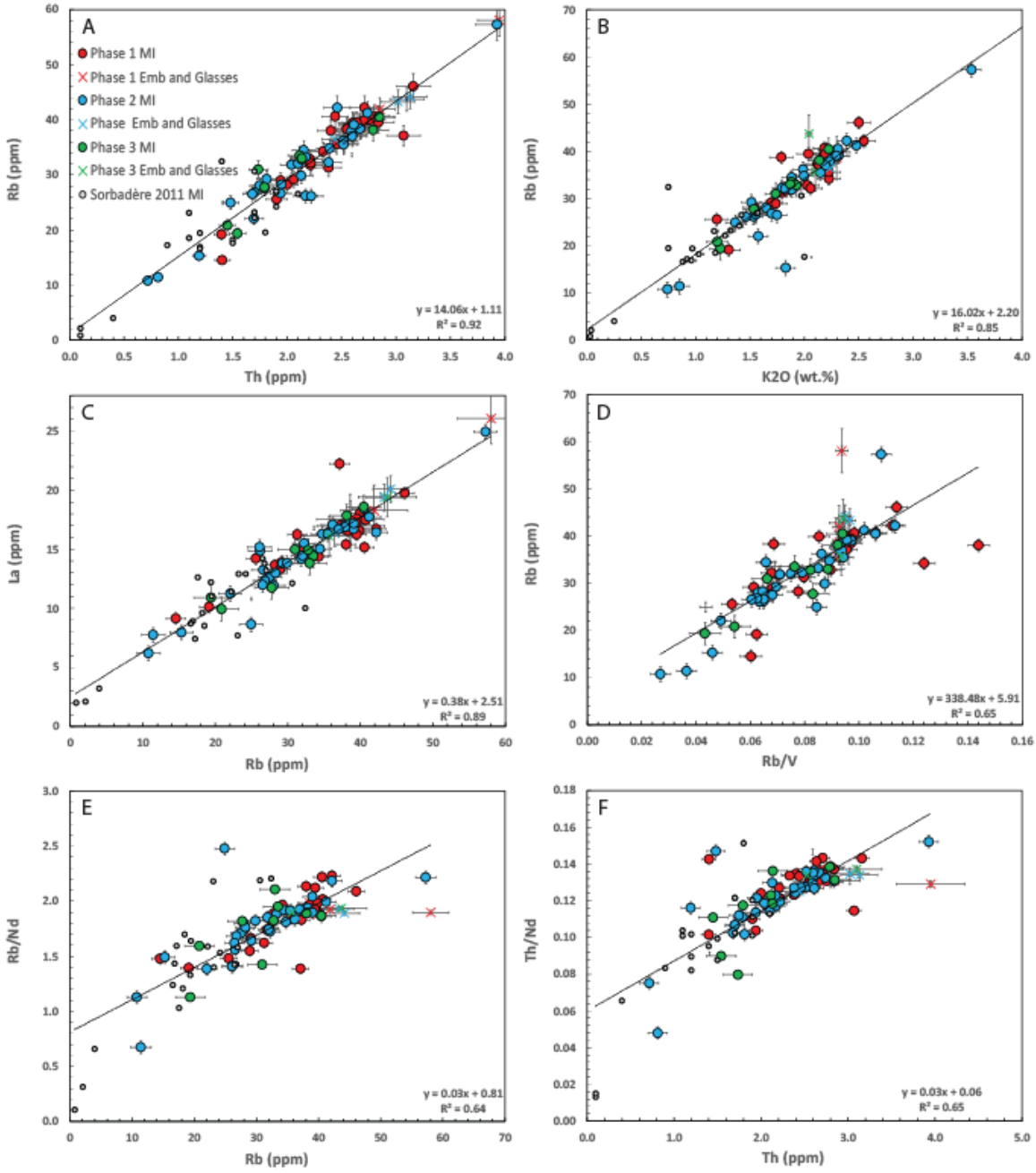

***Figure 7**: Trace element variation diagrams from melt inclusions and matrix glasses from the 2017-2018 eruption (this study; note that olivine-hosted MI are PEC-corrected) and from older deposits (Sorbadere et al. 2011). **A**. Plot of Rb versus Th. **B**. Plot of Rb versus K_2O. **C**. Plot of La versus Rb. **D**. Plot of Rb versus Rb/V. **E**. Plot of Rb/Nd versus Rb. **F**. Plot of Th/Nd versus Th. Linear regression lines through all data are presented on each plot. The data from **A** and **B** define linear trends that passes through the origin as expected for fractional crystallization while data from **C** define a linear correlation that does not pass through the origin, potentially indicative of mixing between two components. Data from **D** is not well explained by a linear relationship (R^2=0.65) as expected for melts related by either mixing or fractional crystallisation. Data from **E** and **F** are not well explained by linear relationships (R^2=0.64 and 0.65 respectively), potentially indicating mixing between two components. On diagram **E** and **F** fractional crystallisation should result in no variations in Rb/Nd and Th/Nd as a function of Rb and Th concentrations respectively.*

458 **Volatiles**

459 In melt inclusions and matrix glasses, chlorine ranges from 1435 to 7243 ppm, fluorine from
460 410 to 779 ppm, water from 0 to 2.2 wt.%, CO_2 from 0 to 3899 ppm and sulfur from 30 to
461 1541 ppm. Both H_2O and CO_2 in melt inclusions have the potential to be altered during post-
462 entrapment processes such as diffusive H^+ exchanges between the MI and the melt through
463 the olivine (e.g., Massare et al. 2002; Danyushevsky et al. 2002; Chen et al. 2011; Gaetani et
464 al. 2012; Bucholz et al. 2013; Portnyagin et al. 2019) or CO_2 diffusion between the MI and its
465 shrinkage bubble (e.g., Anderson and Brown, 1993; Steele-Macinnis *et al.*, 2011; Wallace *et*
466 *al.*, 2015). While there is no evidence for either process in the investigated sample set, neither
467 can be discarded. A conservative approach is hence to consider the measured H_2O and CO_2
468 values as minima. Melt inclusions from phase one tend to be richer in chlorine and fluorine
469 and poorer in water than melt inclusions from phase two and three, with phase three being the
470 poorest in chlorine and fluorine. No systematic differences are observed in the CO_2 and sulfur
471 content of the melt inclusions between the three phases.
472
473 Neither chlorine, fluorine nor CO_2 correlates with Nb despite being theoretically similarly
474 incompatible (Fig. S5A, B and D). Likewise, water does not correlate with Ce despite being
475 theoretically similarly incompatible (Fig. S5C). Finally, the sulfur content does not correlate
476 with FeO content suggesting that sulphide saturation did not take place during the magmatic
477 evolution recorded by melt inclusions. Together all these observations suggest that the
478 volatiles contents of melt inclusions and matrix glasses are not determined by differentiation
479 and must be more reflective of degassing processes even though no clear open- nor closed-
480 system degassing trend is shown by the data. Little correlations are observed between volatile
481 element excepted for water and sulfur (Fig. 8). The majority of the sixty-eight melt inclusions

482 analysed have low CO_2 content, between detection limit (<50) and 500 ppm, while only five
483 inclusions have CO_2 content above 1000 ppm.

484

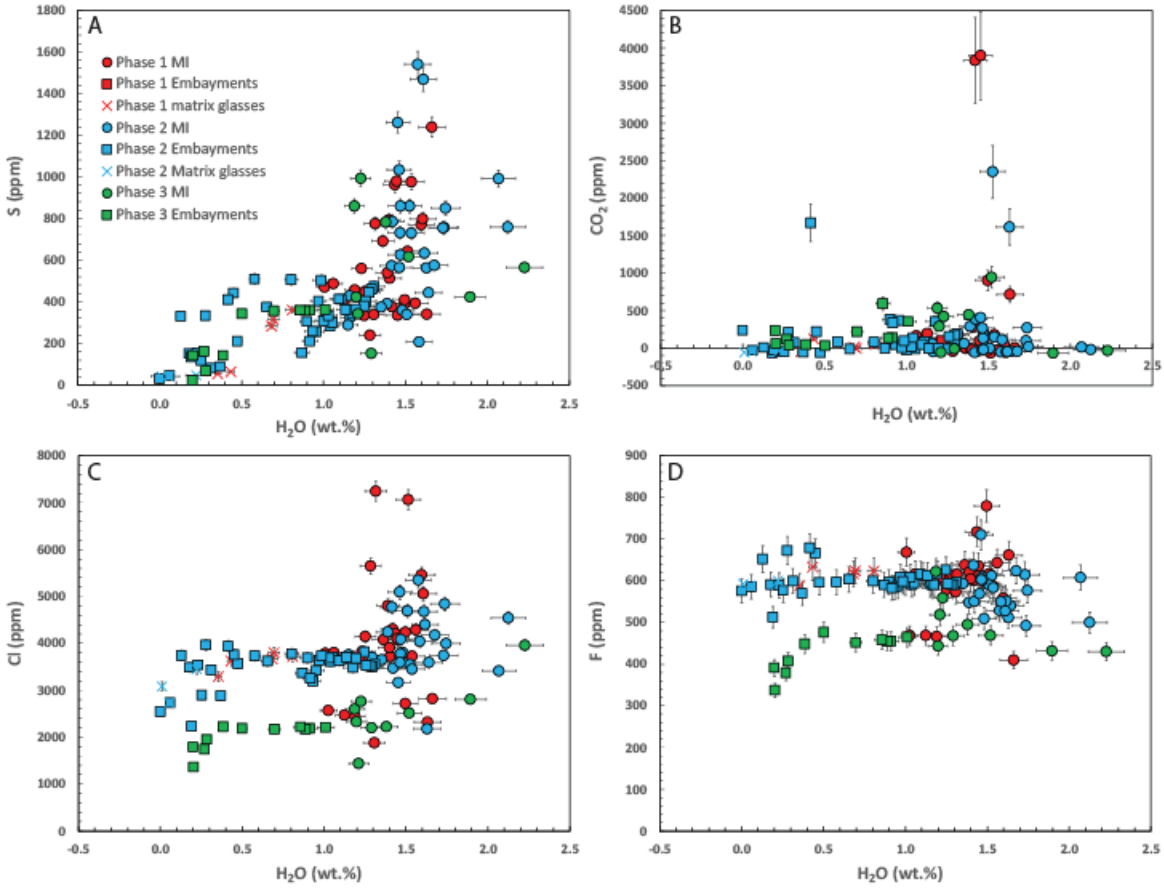

485
486 ***Figure 8****: Volatile elements abundance in melt inclusions, embayments and matrix glasses*
487 *from Ambae.*
488

Geothermobarometry and volatile saturation pressure

The presence of euhedral microlites of plagioclase, clinopyroxene, and olivine indicates that interstitial glasses are saturated with all three phases. Interstitial glasses are in equilibrium with olivine microlite rims (Fe/Mg Kd = 0.27-0.29;Roeder and Emslie 1970), clinopyroxene microlite rims (Fe/Mg Kd = 0.19-0.33; Putirka 2008), and plagioclase microlite rims (Ab/An Kd=0.17-0.32, Putirka 2008). Pre-eruptive temperatures were thus calculated using a variety of mineral-saturation models (Table 1). At least 15 glass compositions were analysed for each phase; for a given phase, all analyses are within analytical error of each other, so only the average value was used for thermobarometry calculations. All these estimates are within error of each other and are consistent with a pre-eruptive temperature of 1145 ± 15 °C, with possibly a small increase of 8 °C between phase 1 and phase 4. These calculations were performed without taking into account the influence of water on mineral-saturation temperatures. Water concentrations in matrix glasses vary between 0.01 and 0.81 wt% (Table S9). Addition of a maximum of 0.81 wt% H_2O results in a 30 °C decrease (Médard and Grove 2008), i.e. a minimum pre-eruptive temperature of 1115 ± 15 °C.

Since interstitial glasses are saturated with olivine, plagioclase and clinopyroxene, it is possible to estimate the equilibration pressure from the pressure-dependence of the olivine-plagioclase-clinopyroxene cotectic (Yang et al. 1996). The calibration of Yang et al. (1996) as implemented by Kelley and Barton (2008) gives pressure estimates of 50 ± 110 MPa, , indicating that the latest stages of crystallization occurred in the upper 6 km of the crust. Given that the bulk rock compositions are also saturated with olivine, plagioclase and clinopyroxene, it is possible to estimate a pressure where the melt equivalent to the bulk rock was extracted using the same method. The average pressure at which fractional crystallization from a more mafic magma produces the bulk rock composition is 133 ± 110 MPa. The model

514 of Kelley and Barton (2008) has been developed for water-poor Icelandic basalts. Addition of
515 water stabilizes clinopyroxene, resulting in pressure estimates that are too high (Husen et al.
516 2016). If interstitial glasses contained water when they last equilibrated with the phenocrysts,
517 the equilibration pressure would be lower, i.e. within error of the surface.
518
519 Crystallization pressures can also be estimated using the pressure-sensitive incorporation of
520 the jadeite component in clinopyroxene (e.g., Putirka, 2008). Barometers have been
521 calibrated either purely from the jadeite component of the clinopyroxene, or from jadeite
522 partitioning between clinopyroxene and melt. This equation is very sensitive to temperature
523 and water concentration in melts, but less sensitive to the exact melt composition. We
524 simultaneously solved for pressure and temperature using equation (30) and (33) of Putirka
525 (2008) to minimize temperature effects. We initially paired microlite and phenocryst rims
526 compositions with matrix glass compositions, phenocryst core compositions with bulk rock
527 compositions, and melt inclusion compositions with their host phenocrysts, and only kept
528 clinopyroxene analyses for which Fe/Mg Kd = 0.28 +/-0.08 (Putirka 2008). Phenocrysts cores
529 are, however, rarely in equilibrium with the bulk composition, and more commonly in near-
530 equilibrium with the matrix glass, so we paired phenocryst core compositions with matrix
531 glasses. This approximation could produce a ~30 MPa error on pressure, much smaller than
532 the accuracy of the barometer. Water concentration in glasses was assumed to be 1.5 wt%,
533 the average water content in melt inclusions, except for melt inclusions in which water
534 concentrations have been analysed. Equilibrium between 11 melt inclusions and their host
535 clinopyroxenes gives pressures between 43 and 326 MPa, with an average pressure of 184 ±
536 75 MPa at an average temperature of 1089 ± 11 °C. The temperature is lower than the
537 temperature estimated from glass thermometry, since it is calculated with a higher water
538 content. Identical pressures and temperatures were obtained from 26 analyses of phenocryst

539 cores (170 ± 86 MPa at 1091 ± 13 °C) and 28 analyses of phenocryst and microlite rims (188
540 ± 73 MPa at 1093 ± 12 °C), with a global average of all pressure calculations of 181 ± 78
541 MPa. Individual pressures vary between 13 and 328 MPa. Interestingly, the use of a
542 clinopyroxene-only barometer (equation 32b of Putirka et al. 2008) produces similar results,
543 with an average of 155 ± 65 MPa. Uncertainties due to barometer calibrations are quite large,
544 with a standard error of estimate of 160 MPa for equation (30) of Putirka (2008). The final
545 pressure estimates of 180 ± 160 MPa indicates that crystallization happened between 1 and
546 12 km, assuming a 2900 $kg.m^{-3}$ density for the basaltic crust. These values are consistent with
547 estimates from melt inclusion volatile elements concentrations, and within error of estimates
548 based on cotectic melt compositions using bulk rock compositions. Pressure estimated from
549 cotectic melt compositions of interstitial glasses are lower and register the latest stages of
550 crystallization, whereas mineral compositions can register earlier, possibly deeper, stages.
551
552 Melt inclusions entrapment pressures were calculated using the model of Iacono-Marziano et
553 al., (2012) for H_2O-CO_2 saturation pressure. They yield entrapment pressures between 20 and
554 427 MPa (Fig. 9), consistent with pressures of 43 to 326 MPa estimated from
555 clinopyroxene/melt barometry. Given the above-reported error on the volatile content
556 determination and the error on the model, the results can conservatively be taken to be
557 accurate at ± 20%. Yet, as discussed previously, H_2O and CO_2 values are to be considered as
558 minimum values due to possible diffusion of both species out of the MI. The entrapment
559 pressures are therefore also to be taken as minimum pressure estimates. The two deepest
560 inclusions are hosted in pyroxenes and their entrapment pressure estimates from volatile
561 saturation (410 and 427 MPa) is fairly consistent, although higher, than their host pyroxene
562 calculated crystallisation pressure (277 and 302 ± 160 MPa). Most other pyroxene-hosted
563 inclusions record volatile saturation pressure lower than their host pyroxene calculated

564 crystallisation pressure yet within the standard error. Saturation pressures are also consistent
565 with the calculated cotectic pressures, and point to a shallow magma storage system
566 somewhere between 0.5 and 3 km depth for most of the crystals.

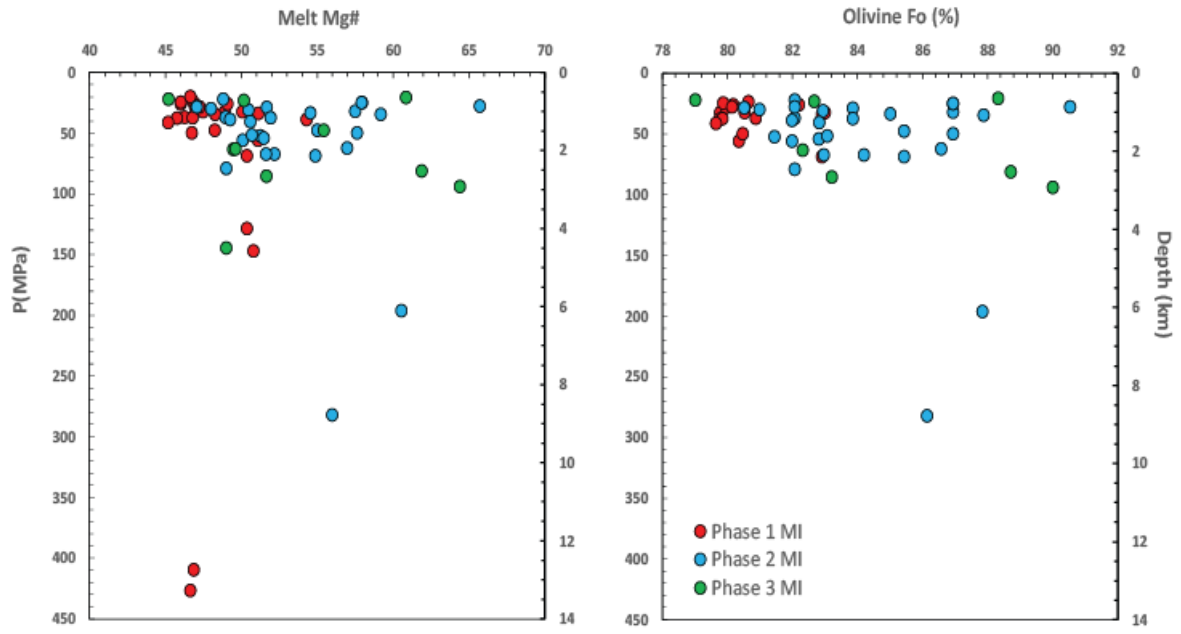

567

568 ***Figure 9****: Melt inclusions entrapment pressure calculated from H_2O-CO_2 saturation*
569 *pressure, compared to melt Mg# and host olivine forsterite content. Note that some of the MI*
570 *are hosted in pyroxenes, hence not plotted on the right-hand side diagram.*
571

572 **Residence time**

573 We modelled the %Fo concentrations of five profiles obtained from two olivine from phase 1
574 and two olivine from phase 2 (Fig. 10). The diffusion model parameters and results are
575 provided in Table 2. For normally zoned phase 1 olivine we determined diffusion timescales
576 ranging from 4 to 185 days. For reversely zoned olivine from phase 2 we determined
577 diffusion timescales ranging from 82 to 293 days (keeping in mind that phase 2 occurred
578 about two months after phase 1). While our dataset is limited, it does already highlight a
579 variety of diffusion timescales recorded by olivine phenocryst/antecryst. These results
580 suggest that the shallow magma chamber has been periodically recharged over the days to
581 year preceding the eruption. The latest recorded recharge event potentially occurred only a
582 few days prior to the eruption while the oldest recorded event occurred about a year before
583 the eruption.

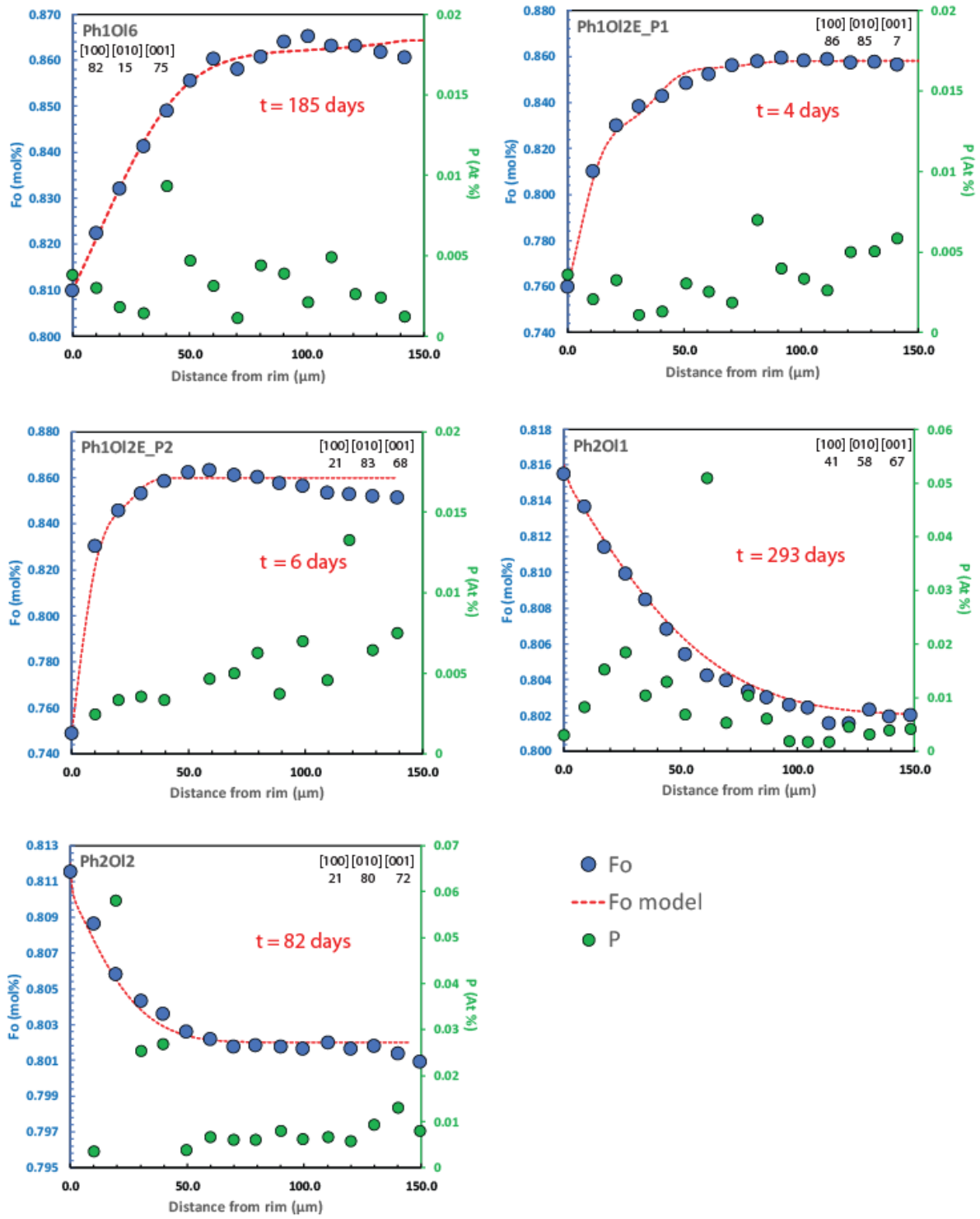

584

585 ***Figure 10***: *Results of diffusion modelling compared to %Fo concentrations profiles*
586 *(measured by EMPA) in two olivine crystals from phase 1 and two olivine crystals from*
587 *phase 2 of the 2017-2018 Ambae eruptions. Modelling was performed using the DIPRA*
588 *software (Girona and Costa 2013). Phosphorus profiles are shown and do not correlate with*
589 *%Fo content as expected for Fe-Mg zoning resulting from diffusion although the error on*
590 *phosphorus measurement (3σ = ±0.002) could partly mask any correlation. Initial conditions*
591 *are shown in Fig. S6.*
592

Ascent rates

Volatile diffusion modelling was performed to match the measured H_2O concentration profiles (obtained by SIMS) along three melt embayments from phase two of the 2017-2018 eruption (note that the olivine used here are different from the ones used for Fe-Mg diffusion modelling in the previous section). Best fit solutions of the diffusion models are shown in Fig. 11 with initial conditions and model parameters given in Table 3. These results give decompression rates of 0.24 ±0.04, 0.25 ±0.06 and 0.55 ±0.20 MPa/s which corresponds to ascent rates in the order of 33-75 km/h, assuming a unique melt/rock density of 2665 $kg.m^{-3}$ for the trachybasaltic magma (Lange and Carmichael 1990). Concentrations of H_2O at the edge of the profiles are 0.06, 0.18, and 0.95 wt% indicating the degassing process can be quenched at about 4 MPa.

Diffusion modelling was also performed to reproduce S and Cl concentration profiles (obtained by SIMS). However, the measured profiles showed S and Cl concentrations at the edge of the embayments and in the surrounding matrix glass, that are much higher than expected for equilibrium at 0.1 MPa (i.e., ~50 to 200 ppm S and > 3400 ppm Cl remaining). This suggests that decompression rates were too high for S and Cl to maintain equilibrium during degassing, resulting in oversaturation of these species in the melt, as shown experimentally for CO_2 (Pichavant et al. 2013).

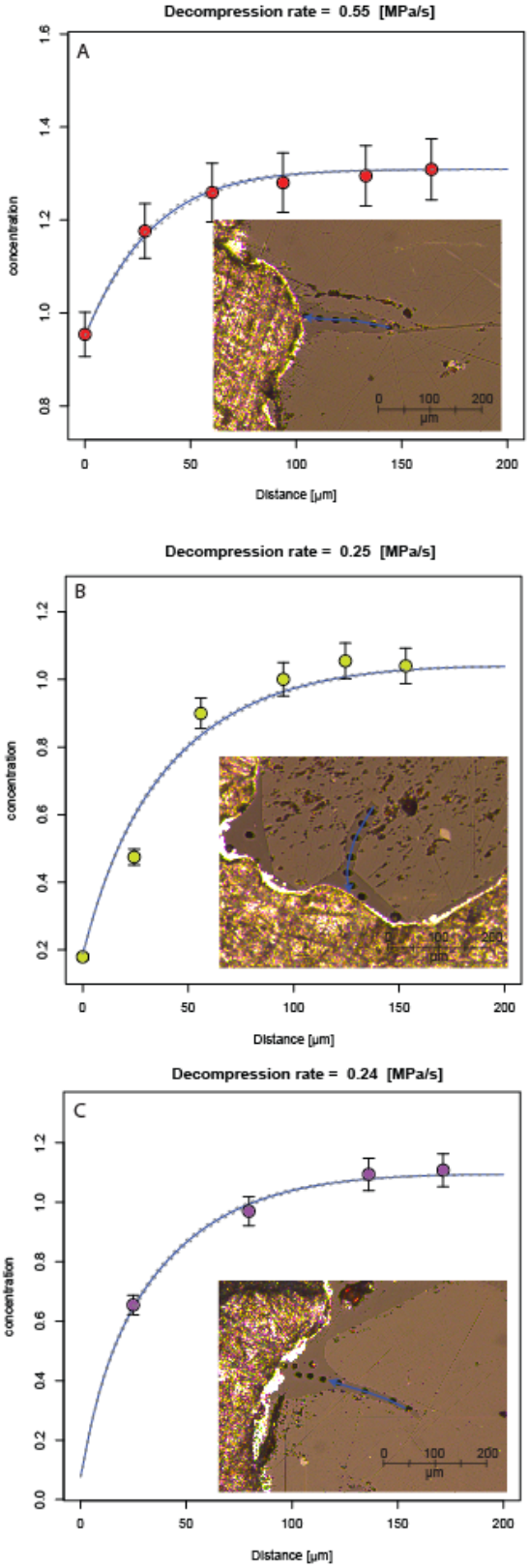

613

614 ***Figure 11****: Results of diffusion modelling compared to H_2O concentration (measured by*
615 *SIMS) in three melt embayments from phase two of the 2017-2018 Ambae eruptions. Insets*
616 *show microphotograph of each embayment with blue arrows marking the location of the*
617 *SIMS analyses.*

618
619 Ascent rates can also be estimated from the microlite density (Toramaru et al. 2008). The
620 number and nature of microlites is extremely similar between samples of phases 1, 2 and 3
621 (Fig. S7). A higher number of microlites is observed in ashes from phase 4, but this is mainly
622 due to the abundance of very small microlites that are not observed in other phases. These
623 microlites might have crystallized during eruption. 2D microlite number densities and phase
624 proportions were estimated using BSE images. This allowed us to compute average microlite
625 sizes using the method of Hammer et al. (1999). To calculate 3D microlite number densities,
626 we then divided the 2D microlite number densities by the average microlite size. For samples
627 from phase 1, average microlite number densities averaged on seven BSE images are $3.8.10^{13}$
628 m^{-3} for plagioclase, $9.7.10^{12}$ m^{-3} for clinopyroxene, and $1.8.10^{12}$ m^{-3} for olivine. Given the
629 small number of crystals (2 to 10 per image), the olivine MND has a very large uncertainty,
630 and will not be taken into account. Using a maximum volatile content at microlite nucleation
631 of 2.23 wt% H_2O (highest measurement in melt inclusions) results in decompression rates of
632 $1.6.10^5$ $Pa.s^{-1}$ and $1.1.10^5$ $Pa.s^{-1}$ calculated from plagioclase and clinopyroxene, respectively.
633 The density of the trachybasaltic magma is 2665 $kg.m^{-3}$ (Lange and Carmichael 1990),
634 producing ascent rates of 4-6 $m.s^{-1}$., or 15-23 $km.h^{-1}$, consistent with values determined from
635 volatile diffusion.
636

637 # DISCUSSION

638 **The Ambae plumbing system**

639 Clinopyroxene crystallisation pressures and melt inclusions entrapment pressures both
640 suggest that the magma involved in the 2017-2018 Ambae eruption had been crystallising
641 pyroxene and olivine at depths of 0.5 to 14 km minimum. Most melt inclusions, however,
642 record low entrapment pressures corresponding to depth of 0.5 to 3 km. This suggest that
643 most of the erupted magma originated from a shallow magma chamber located at sea level

644 (Fig. 12). There is no relationship between the melt inclusions entrapment pressures and
645 markers of magmatic differentiation (Fig. 9), suggesting that the plumbing system is not
646 arranged in a succession of progressively shallower and more evolved magma chambers.
647 Instead, multiple chambers of variously differentiated magma must occupy similar depth
648 levels, following horizontally separated pathways (Fig. 12).

649

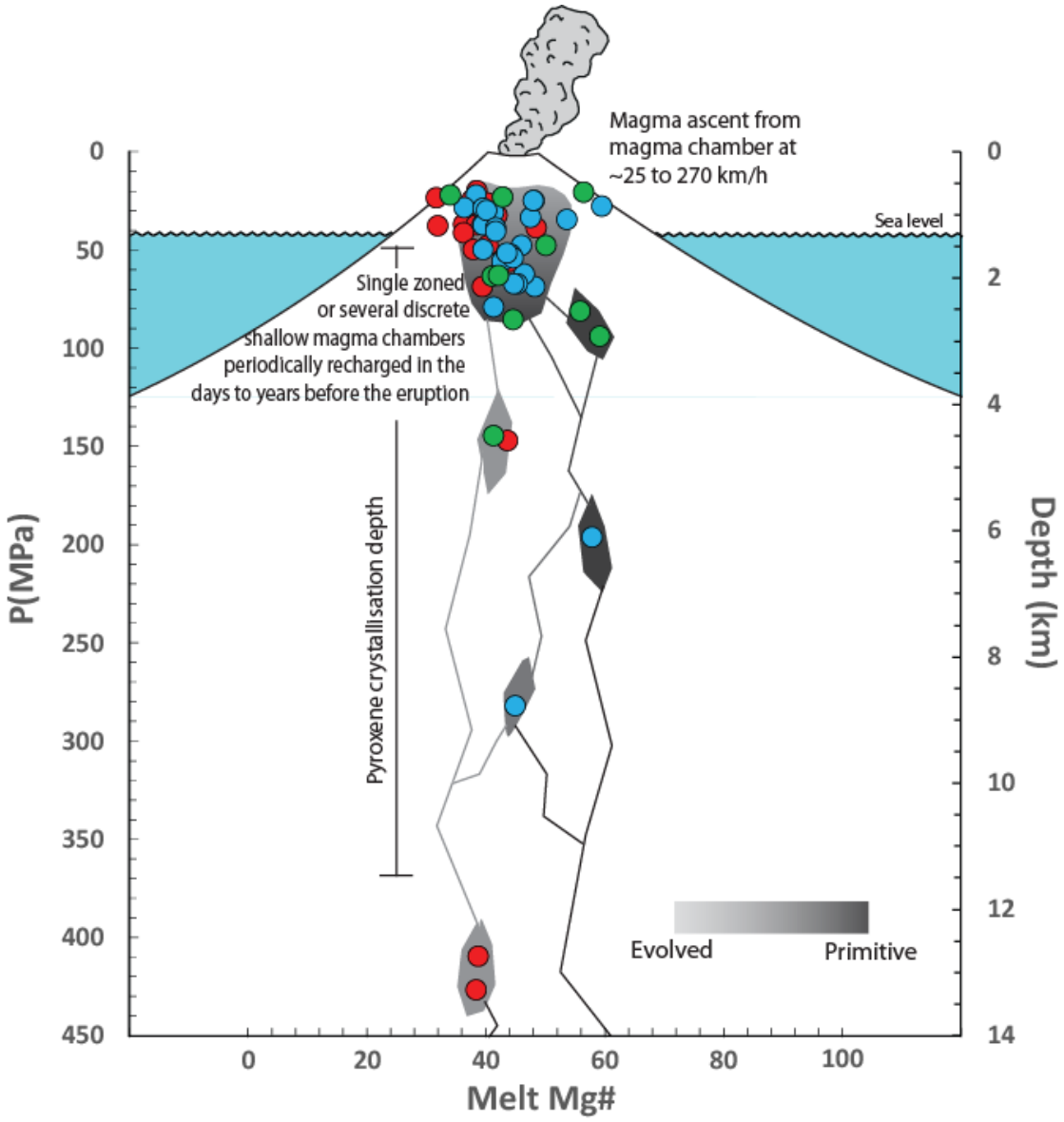

650

651 ***Figure 12****: Schematic representation of the Ambae plumbing system on which melt inclusions*
652 *entrapment pressure and Mg# are overlaid. Magmas at different stages of differentiation*
653 *migrate through the crust and mix via episodic recharge events in a shallow magma chamber*
654 *located at sea level. During the eruption, evolved magma is emptied preferentially towards*

655 *the beginning while more primitive magma is erupted during later phases. Note that there is*
656 *no relationship between Mg# and horizontal coordinates of the melts.*
657

658 **The 2017-2018 emptying of Ambae's plumbing system**

659 The 2017-2018 eruption started with phreatic activity and the creation of a small pyroclastic
660 cone at the lake centre several days before the first appearance of phase one lava at the
661 surface (Bani et al., in prep). A phreatic or phreatomagmatic start to a magmatic eruption is a
662 commonly observed occurrence at volcanoes with previously-closed conduits, examples
663 include the 1955 Bezymianny (Gorshkov 1959), 1980 Mt St Helens (Lipman and Mullineaux
664 1981), 1990 Kelut (Bourdier et al. 1997), 1990–1995 Unzen (Nakada et al. 1999) and 2017-
665 ongoing Nevados de Chillan (Moussallam et al. 2018) eruptions. Even if they do not
666 necessarily lead to edifice destruction (e.g., 1888 Bandai eruption, Yamamoto et al. 1999),
667 phreatic events can vaporize and expel water in shallow aquifers, unloading the upper crust
668 hence changing the stress field around, and the magmatic pressure within, a magma reservoir
669 (Pinel and Jaupart 2005). As such, phreatic events can act as trigger or facilitate magmatic
670 eruptions. Given the delay observed between the phreatic eruptions (6 September 2017) and
671 magma arrival at the surface (22 September 2017), it is conceivable that the phreatic
672 eruptions played a role in favouring the magmatic ones, although it is likely that the phreatic
673 eruptions themselves were driven by magmatic gases given the large quantities of SO_2 they
674 released (Bani et al., in prep.).
675

676 Bulk rocks, matrix glasses and melt inclusions from phase one are compositionally more
677 evolved than those of phase two and three (Fig. 5 and 6). Melt inclusions from phase two and
678 three have higher Mg#, MgO, CaO content, lower Si and Al content and tend to be hosted in
679 more forsteritic olivine (Fig. 6). An overlap in composition exist however between the three
680 phases such that phase two and three, whilst dominated by more primitive melt inclusions, do

681 also contain inclusions that have similar compositions as the ones from phase one. Normal
682 zoning of olivine and pyroxene phenocrysts is most commonly observed in the early and late
683 phases of the eruption, yet reverse zoning is common also shown by a number of crystals,
684 particularly in phase 2 and 3 (Fig. 2, 3 and 10). The observed compositional continuity (as
685 opposed to a bimodal distribution) shown by the melt inclusions, from primitive to evolved
686 end members (Fig. 5,6) suggest a simple magmatic evolution with all erupted melts related by
687 simple liquid line of descent from the same primitive parental magma (potentially similar to
688 the 8 to 14 wt.% MgO melts described by Sorbadère et al. 2011) (Fig. 6). Trace element
689 variation diagrams from melt inclusions and matrix glasses (Fig. 7) show a strong linear
690 correlation between Rb, Th and K_2O (highly incompatible elements) that points towards the
691 origin as expected for melts related by fractional crystallisation. This again suggests that all
692 melt inclusion compositions (including from older lavas) are consistent with simple fractional
693 crystallisation evolution from a single parental magma.
694
695 Some trace element systematic do hint at mixing processes having taken place. A strong
696 linear correlation is evident between La and Rb (Fig. 7C) but a regression through the data
697 does not pass through the origin potentially indicative of mixing between two components
698 (e.g., Schiano et al. 2010). Plots of Rb/Nd versus Rb and Th/Nd vs Th (Fig. 7E and F) define
699 trends that are not well described by linear relationships suggesting again mixing between
700 two components. On these diagrams, simple fractional crystallisation would result in no
701 variations in Rb/Nd and Th/Nd as a function of Rb and Th concentrations respectively (e.g.,
702 Schiano et al. 2010). In addition, the fact that numerous olivine crystals exhibit reverse
703 zoning and the bi-modal distribution observed in olivine forsterite content with a significant
704 proportion of phase 2 and 3 olivine recording core Fo content higher in magnesium than

705 expected for equilibrium with the bulk rock (Fig. 4), both suggest that some of the olivine are
706 antecrystic and that some amount of mixing has taken place.
707
708 Diffusion timescales from olivine zoning show multiple recharge events occurring a few days
709 to a year prior to the 2017-2018 eruption (exact timescale depending on initial conditions). It
710 is possible therefore that the latest recharge event played a role in triggering (via magmatic
711 gas release) the initial phreatic and subsequent magmatic activity as the timing (a few days
712 before phase 1 eruption) is consistent with the onset of phreatic and seismic activity.
713
714 Based on all these observations we suggest that:

715 1. The Ambae plumbing system was periodically recharged by co-genetic magmatic
716 batches in the days to year prior to eruption.
717 2. The initial phreatic activity, propelled by magmatic gases, likely opened a pathway or
718 modified the local stress field allowing pressurized magma to travel to the surface.
719 3. The eruption first taped into the most evolved magma chamber(s) erupting phase one
720 magma. As the eruption progresses from phase one to four, the most evolved
721 chamber(s) got progressively exhausted opening the way to more primitive (and yet
722 not necessarily deeper) magma from other chambers.
723 4. During or prior to the eruption some small amount of mixing between co-genetic
724 magmas from different chambers occurred.

725
726 **Magma ascent rate**
727 Modelling of volatile diffusion profiles in melt embayments suggest magma decompression
728 rates in the order of 0.24 to 0.55 MPa/s, corresponding to ascent rates of 9 to 21 m/s (33 to 75
729 km/h) while calculated decompression rates based on microlite number densities are in the

730 order 0.11 to 0.16 MPa/s corresponding to ascent rates of 4 to 6 m/s (15 to 23 km/h).
731 Considering that the two methods are entirely independent their broad agreement is worth
732 highlighting and brings confidence in the determined values. Given a shallow magma
733 chamber at 0.5 to 3 km depth, it must hence have taken 24 to 122 seconds for the magma to
734 travel from the top of the magma chamber to the surface. The decompression and ascent rates
735 we calculate are comparable to other volcanoes using the same embayment volatile diffusion
736 modelling method. Liu et al., (2007) investigated the 26.5 ka phreatomagmatic Oruanui
737 eruption of Taupo (New Zealand) and found a decompression rate of 0.001 to 0.007 MPa/s.
738 Myers et al., (2018) investigated the 25.4 ka Oruanui eruption of Taupo, 0.767 Ma Bishop
739 Tuff and 2.08 Ma Huckleberry Tuff and found decompression rates in the order of 10^{-3} to 10^{-1}
740 MPa/s. Humphreys et al., (2008) found decompression rates of 0.9-1.6 MPa/s for the 1980
741 Plinian eruption of Mount St Helens, (Washington, USA). Lloyd et al., (2014) found
742 decompression rate of 0.3 to 0.5 MPa/s for the basaltic andesite sub-Plinian eruption of
743 Volcán de Fuego (Guatemala) while Ferguson et al., (2016) found decompression rates
744 between 0.05 and 0.45 MPa/s during fire fountain to sub-Plinian basaltic eruptions at Kīlauea
745 volcano (Hawaii, USA). Figure 13 shows a compilation of currently available magmatic
746 decompression rate estimated using the embayment volatile diffusion method and compares it
747 to eruption magnitude. For basaltic eruptions a trend seems to emerge of increasing
748 decompression rate (i.e. ascent rate) with increasing eruption magnitude. The trend however
749 does not extend to more silicic and higher magnitude eruptions with the largest, ultraplinian,
750 eruptions yielding comparatively slow decompression rates.
751
752
753
754

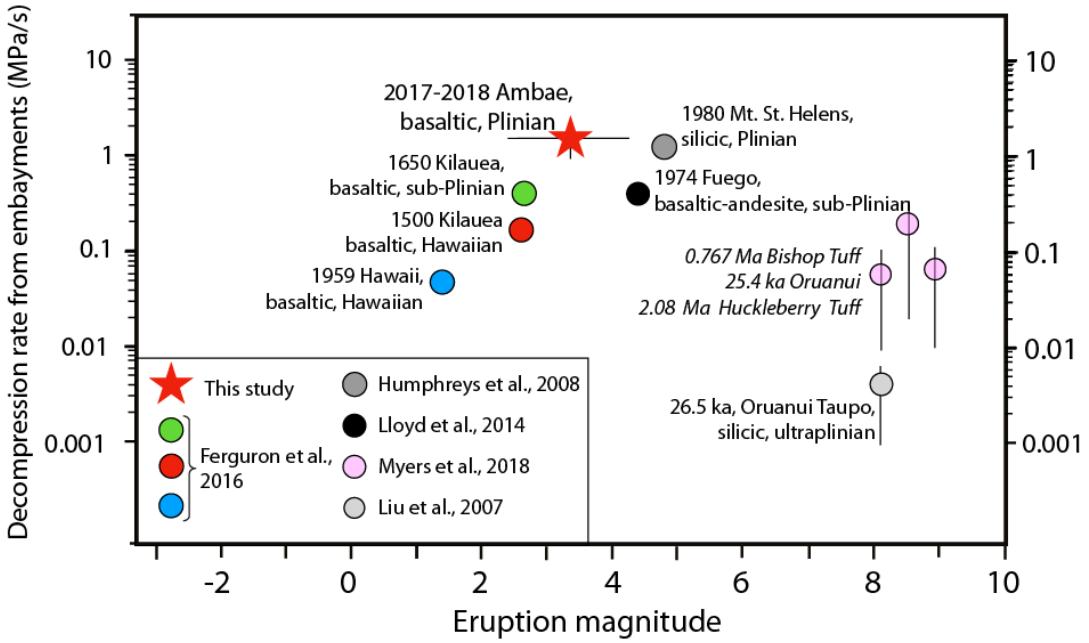

***Figure 13**: Compilation of decompression rate estimates using the embayment volatile diffusion method and comparison with eruption magnitude. For basaltic eruptions a trend of increasing decompression rate (i.e. ascent rate) with increasing eruption magnitude can be observed. The trend however does not extend to more silicic and higher magnitude eruptions.*

Calculated magma ascent rate is strongly influenced by a parameter that is difficult to assess: the amount of pre-existing fluid/bubble before the onset of the final eruptive ascent (Ferguson et al., 2016). This is because the curve of the H_2O depletion with respect to pressure varies towards deeper degassing with more pre-existing fluid (see Fig. S1). While Ferguson et al. (2016) used H_2O-CO_2-S profiles to simultaneously constrain this parameter, it was not possible for the case here as CO_2, S and Cl show significant disequilibrium (super-saturation compared to H_2O). The values reported here are minimum ascent rate with pre-existing fluid mass of 0 %. Supposing a value of fluid mass of 1 %, the ascent rate increases by approximately a factor of 2.5. As the volatile element abundances in the melt inclusions are somewhat higher than the highest value of the embayments, an estimated pre-existing fluid mass of 0.5 to 1.5 % could be close to reality. A faster magma ascent rate is furthermore consistent with the strong disequilibrium recorded in slower diffusing elements (CO_2, S, Cl). The magma ascent rate can hence be estimated to be in the order of 1-2 MPa/s.

774

775 Considering pre-eruptive volatiles in our calculations, magma ascent rate during the 2017-
776 2018 Ambae eruption therefore appears as one of the fastest among other eruptions where the
777 same methodology has been applied (Liu et al. 2007; Humphreys et al. 2008; Lloyd et al.
778 2014; Ferguson et al. 2016). This fast ascent was likely propelled by pre-eruptive volatiles,
779 consistent with observations that the eruption reached the lower stratosphere (NASA Earth
780 Observatory 2019) and released extremely large amounts of gases into the atmosphere (2.08
781 Tg of SO_2 in the first nine months, equivalent to a third of the atmospheric loading from the
782 1982 El Chichon eruption) while expelling relatively minor amounts of solid materials during
783 the same period (Bani et al., in prep).

784

785 # CONCLUSIONS

786 The 2017-2018 eruption of Ambae (Aoba) volcano was the largest recorded event in Vanuatu
787 since the 1929 eruption of Ambrym. It expelled large quantities of gases to the atmosphere
788 and prompted local authorities to evacuate the 11,000 inhabitants of the islands making it the
789 largest volcanic disaster in the country's recorded history. In this contribution we used major,
790 trace and volatile elements in bulk rocks, matrix glasses, melt inclusions, embayments and
791 minerals to shed light on the magmatic processes operating during this eruption. We found
792 that (i) The Ambae plumbing system was periodically recharged by magmatic batches in the
793 year prior to eruption with the latest recharge event occurring only a few days before
794 eruption. (ii) the eruption was likely facilitated by an initial phase of phreatic activity, itself
795 triggered by magmatic gases potentially associated with the latest magmatic recharge event.
796 (iii) The magma released during the eruption started crystallising at 14 to 5 km depth before
797 residing in a shallow magma chamber, located at ~0.5 to 3 km depth. (iv) From the shallow
798 magma chamber to the surface, minimum magma decompression rate ranges from 0.11 to

799 0.55 MPa/s, with a possible actual rate of 1-2 MPa/s, corresponding to average ascent rates in
800 the order of 15 to 270 km/h and a travel time between the top of the shallow reservoir and the
801 surface of 9 seconds to 2 minutes. Such a fast ascent rate, together with the high eruptive
802 plume heights (reaching the lower stratosphere) and the large quantities of SO_2 released,
803 suggest that a large amount of pre-eruptive volatiles must have been present in the reservoir.

804 # REFERENCES

805 Albert H, Costa F, Di Muro A, et al (2019) Magma interactions, crystal mush formation,
806 timescales, and unrest during caldera collapse and lateral eruption at ocean island
807 basaltic volcanoes (Piton de la Fournaise, La Réunion). Earth Planet Sci Lett
808 515:187–199. doi: 10.1016/j.epsl.2019.02.035

809 Allard P, Aiuppa A, Bani P, et al (2016) Prodigious emission rates and magma degassing
810 budget of major, trace and radioactive volatile species from Ambrym basaltic
811 volcano, Vanuatu island Arc. J Volcanol Geotherm Res 322:119–143. doi:
812 10.1016/j.jvolgeores.2015.10.004

813 Almeev RR, Holtz F, Koepke J, Parat F (2012) Experimental calibration of the effect of H2O
814 on plagioclase crystallization in basaltic melt at 200 MPa. Am Mineral 97:1234–1240.
815 doi: 10.2138/am.2012.4100

816 Anderson AT, Brown GG (1993) CO_2 contents and formation pressures of some Kilauean
817 melt inclusions. Am Mineral 78:794–803

818 Bani P, Join J-L, Cronin SJ, et al (2009a) Characteristics of the summit lakes of Ambae
819 volcano and their potential for generating lahars. Nat Hazards Earth Syst Sci 9:1471–
820 1478. doi: 10.5194/nhess-9-1471-2009

821 Bani P, Oppenheimer C, Varekamp JC, et al (2009b) Remarkable geochemical changes and
822 degassing at Voui crater lake, Ambae volcano, Vanuatu. J Volcanol Geotherm Res
823 188:347–357. doi: 10.1016/j.jvolgeores.2009.09.018

824 Bénard A, Klimm K, Woodland AB, et al (2018) Oxidising agents in sub-arc mantle melts
825 link slab devolatilisation and arc magmas. Nat Commun 9:3500. doi: 10.1038/s41467-
826 018-05804-2

827 Bourdier J-L, Pratomo I, Thouret J-C, et al (1997) Observations, stratigraphy and eruptive
828 processes of the 1990 eruption of Kelut volcano, Indonesia. J Volcanol Geotherm Res
829 79:181–203. doi: 10.1016/S0377-0273(97)00031-0

830 Bouvier A-S, Métrich N, Deloule E (2008) Slab-Derived Fluids in the Magma Sources of St.
831 Vincent (Lesser Antilles Arc): Volatile and Light Element Imprints. J Petrol 49:1427–
832 1448. doi: 10.1093/petrology/egn031

833 Bucholz CE, Gaetani GA, Behn MD, Shimizu N (2013) Post-entrapment modification of
834 volatiles and oxygen fugacity in olivine-hosted melt inclusions. Earth Planet Sci Lett
835 374:145–155. doi: 10.1016/j.epsl.2013.05.033

836 Chen Y, Provost A, Schiano P, Cluzel N (2011) The rate of water loss from olivine-hosted
837 melt inclusions. Contrib Mineral Petrol 162:625–636. doi: 10.1007/s00410-011-0616-
838 5

839 Collot JY, Daniel J, Burne RV (1985) Recent tectonics associated with the subduction/
840 collision of the d'entrecasteaux Zone in the central New Hebrides. Tectonophysics
841 112:325–356. doi: 10.1016/0040-1951(85)90185-4

842 Daniel J, Gérard M, Mauffret A, et al (1989) Déformation compressive d'un bassin intra-arc
843 dans un contexte de collision ride/arc□: le bassin d'Aoba, arc des Nouvelles-
844 Hébrides. Comptes Rendus Académie Sci 2 Mécanique 308:239–245

845 Danyushevsky LV, McNeill AW, Sobolev AV (2002) Experimental and petrological studies
846 of melt inclusions in phenocrysts from mantle-derived magmas: an overview of
847 techniques, advantages and complications. Chem Geol 183:5–24. doi: 10.1016/S0009-
848 2541(01)00369-2

849 Eggins SM (1993) Origin and differentiation of picritic arc magmas, Ambae (Aoba),
850 Vanuatu. Contrib Mineral Petrol 114:79–100. doi: 10.1007/BF00307867

851 Ferguson DJ, Gonnermann HM, Ruprecht P, et al (2016) Magma decompression rates during
852 explosive eruptions of Kīlauea volcano, Hawaii, recorded by melt embayments. Bull
853 Volcanol 78:71. doi: 10.1007/s00445-016-1064-x

854 Firth C, Handley H, Turner S, et al (2016) Variable Conditions of Magma Storage and
855 Differentiation with Links to Eruption Style at Ambrym Volcano, Vanuatu. J Petrol
856 57:1049–1072. doi: 10.1093/petrology/egw029

857 Gaetani GA, O'Leary JA, Shimizu N, et al (2012) Rapid reequilibration of H2O and oxygen
858 fugacity in olivine-hosted melt inclusions. Geology 40:915–918. doi:
859 10.1130/G32992.1

860 Ghiorso MS, Hirschmann MM, Reiners PW, Kress VC (2002) The pMELTS: A revision of
861 MELTS for improved calculation of phase relations and major element partitioning
862 related to partial melting of the mantle to 3 GPa. Geochem Geophys Geosystems 3:1–
863 35. doi: 10.1029/2001GC000217

864 Girona T, Costa F (2013) DIPRA: A user-friendly program to model multi-element diffusion
865 in olivine with applications to timescales of magmatic processes. Geochem Geophys
866 Geosystems 14:422–431. doi: 10.1029/2012GC004427

867 Gorshkov GS (1959) Gigantic eruption of the volcano bezymianny. Bull Volcanol 20:77–
868 109. doi: 10.1007/BF02596572

869 Gorton MP (1977) The geochemistry and origin of quaternary volcanism in the New
870 Hebrides. Geochim Cosmochim Acta 41:1257–1270. doi: 10.1016/0016-
871 7037(77)90071-0

872 Hammer JE, Cashman KV, Hoblitt RP, Newman S (1999) Degassing and microlite
873 crystallization during pre-climactic events of the 1991 eruption of Mt. Pinatubo,
874 Philippines. Bull Volcanol 60:355–380. doi: 10.1007/s004450050238

875 Hauri E, Wang J, Dixon JE, et al (2002) SIMS analysis of volatiles in silicate glasses: 1.
876 Calibration, matrix effects and comparisons with FTIR. Chem Geol 183:99–114. doi:
877 10.1016/S0009-2541(01)00375-8

878 Hier□Majumder S, Anderson IM, Kohlstedt DL (2005) Influence of protons on Fe-Mg
879 interdiffusion in olivine. J Geophys Res Solid Earth 110:. doi:
880 10.1029/2004JB003292

881 Humphreys MCS, Menand T, Blundy JD, Klimm K (2008) Magma ascent rates in explosive
882 eruptions: Constraints from H2O diffusion in melt inclusions. Earth Planet Sci Lett
883 270:25–40. doi: 10.1016/j.epsl.2008.02.041

884 Husen A, Almeev RR, Holtz F (2016) The Effect of H2O and Pressure on Multiple
885 Saturation and Liquid Lines of Descent in Basalt from the Shatsky Rise. J Petrol
886 57:309–344. doi: 10.1093/petrology/egw008

887 Iacono-Marziano G, Morizet Y, Le Trong E, Gaillard F (2012) New experimental data and
888 semi-empirical parameterization of H2O–CO2 solubility in mafic melts. Geochim
889 Cosmochim Acta 97:1–23. doi: 10.1016/j.gca.2012.08.035

890 Jarosewich E, Nelen J a., Norberg JA (1980) Reference Samples for Electron Microprobe
891 Analysis*. Geostand Newsl 4:43–47. doi: 10.1111/j.1751-908X.1980.tb00273.x

892 Jochum KP, Stoll B, Herwig K, et al (2006) MPI-DING reference glasses for in situ
893 microanalysis: New reference values for element concentrations and isotope ratios.
894 Geochem Geophys Geosystems 7:. doi: 10.1029/2005GC001060

895 Kamenetsky VS, Everard JL, Crawford AJ, et al (2000) Enriched End-member of Primitive
896 MORB Melts: Petrology and Geochemistry of Glasses from Macquarie Island (SW
897 Pacific). J Petrol 41:411–430. doi: 10.1093/petrology/41.3.411

898 Kelley DF, Barton M (2008) Pressures of Crystallization of Icelandic Magmas. J Petrol
899 49:465–492. doi: 10.1093/petrology/egm089

900 Kress VC, Carmichael ISE (1991) The compressibility of silicate liquids containing Fe2O3
901 and the effect of composition, temperature, oxygen fugacity and pressure on their
902 redox states. Contrib Mineral Petrol 108:82–92. doi: 10.1007/BF00307328

903 Lange RA, Carmichael ISE (1990) Thermodynamic properties of silicate liquids with
904 emphasis on density, thermal expansion and compressibility. Rev Mineral Geochem
905 24:25–64

906 Le Voyer M, Rose-Koga EF, Shimizu N, et al (2010) Two Contrasting H2O-rich
907 Components in Primary Melt Inclusions from Mount Shasta. J Petrol 51:1571–1595.
908 doi: 10.1093/petrology/egq030

909 Lipman P, Mullineaux D (1981) The 1980 eruptions of Mount St. Helens, Washington. U.S.
910 Dept. of the Interior, U.S. Geological Survey, Washington

911 Liu Y, Anderson AT, Wilson CJN (2007) Melt pockets in phenocrysts and decompression
912 rates of silicic magmas before fragmentation. J Geophys Res Solid Earth 112:. doi:
913 10.1029/2006JB004500

914 Lloyd AS, Ruprecht P, Hauri EH, et al (2014) NanoSIMS results from olivine-hosted melt
915 embayments: Magma ascent rate during explosive basaltic eruptions. J Volcanol
916 Geotherm Res 283:1–18. doi: 10.1016/j.jvolgeores.2014.06.002

917 Massare D, Métrich N, Clocchiatti R (2002) High-temperature experiments on silicate melt
918 inclusions in olivine at 1 atm: inference on temperatures of homogenization and H2O
919 concentrations. Chem Geol 183:87–98. doi: 10.1016/S0009-2541(01)00373-4

920 Médard E, Grove TL (2008) The effect of H2O on the olivine liquidus of basaltic melts:
921 experiments and thermodynamic models. Contrib Mineral Petrol 155:417–432. doi:
922 10.1007/s00410-007-0250-4

923 Moore G, Vennemann T, Carmichael ISE (1998) An empirical model for the solubility of H 2
924 O in magmas to 3 kilobars. Am Mineral 83:36–42. doi: 10.2138/am-1998-1-203

925 Mosbah M, Metrich N, Massiot P (1991) PIGME fluorine determination using a nuclear
926 microprobe with application to glass inclusions. Nucl Instrum Methods Phys Res Sect
927 B Beam Interact Mater At 58:227–231. doi: 10.1016/0168-583X(91)95592-2

928 Moussallam Y, Bani P, Schipper CI, et al (2018) Unrest at the Nevados de Chillán volcanic
929 complex: a failed or yet to unfold magmatic eruption? Volcanica 1:19–32. doi:
930 10.30909/vol.01.01.1932

931 Moussallam Y, Oppenheimer C, Scaillet B, et al (2015) Megacrystals track magma
932 convection between reservoir and surface. Earth Planet Sci Lett 413:1–12. doi:
933 10.1016/j.epsl.2014.12.022

934 Myers ML, Wallace PJ, Wilson CJN, et al (2018) Ascent rates of rhyolitic magma at the
935 onset of three caldera-forming eruptions. Am Mineral 103:952–965. doi: 10.2138/am-
936 2018-6225

937 Nakada S, Shimizu H, Ohta K (1999) Overview of the 1990–1995 eruption at Unzen
938 Volcano. J Volcanol Geotherm Res 89:1–22. doi: 10.1016/S0377-0273(98)00118-8

939 NASA Earth Observatory (2019) The Biggest Eruption of 2018 Was Not Where You Think.
940 https://earthobservatory.nasa.gov/images/144593/the-biggest-eruption-of-2018-was-
941 not-where-you-think. Accessed 4 Mar 2019

942 Nemeth K, Cronin SJ, Charley DT, et al (2006) Exploding lakes in Vanuatu - “Surtseyan-
943 style” eruptions witnessed on Ambae Island

944 Óladóttir BA, Sigmarsson O, Larsen G, Thordarson T (2008) Katla volcano, Iceland: magma
945 composition, dynamics and eruption frequency as recorded by Holocene tephra layers.
946 Bull Volcanol 70:475–493. doi: 10.1007/s00445-007-0150-5

947 Pichavant M, Carlo ID, Rotolo SG, et al (2013) Generation of CO2-rich melts during basalt
948 magma ascent and degassing. Contrib Mineral Petrol 166:545–561. doi:
949 10.1007/s00410-013-0890-5

950 Pinel V, Jaupart C (2005) Some consequences of volcanic edifice destruction for eruption
951 conditions. J Volcanol Geotherm Res 145:68–80. doi:
952 10.1016/j.jvolgeores.2005.01.012

953 Portnyagin M, Mironov N, Botcharnikov R, et al (2019) Dehydration of melt inclusions in
954 olivine and implications for the origin of silica-undersaturated island-arc melts. Earth
955 Planet Sci Lett 517:95–105. doi: 10.1016/j.epsl.2019.04.021

956 Putirka KD (2008) Thermometers and Barometers for Volcanic Systems. Rev Mineral
957 Geochem 69:61–120. doi: 10.2138/rmg.2008.69.3

958 Roeder PL, Emslie RF (1970) Olivine-liquid equilibrium. Contrib Mineral Petrol 29:275–
959 289. doi: 10.1007/BF00371276

960 Rose-Koga EF, Koga KT, Hamada M, et al (2014) Volatile (F and Cl) concentrations in
961 Iwate olivine-hosted melt inclusions indicating low-temperature subduction. Earth
962 Planets Space 66:81. doi: 10.1186/1880-5981-66-81

963 Rose-Koga EF, Koga KT, Schiano P, et al (2012) Mantle source heterogeneity for South
964 Tyrrhenian magmas revealed by Pb isotopes and halogen contents of olivine-hosted
965 melt inclusions. Chem Geol 334:266–279. doi: 10.1016/j.chemgeo.2012.10.033

966 Ruth DCS, Costa F, Maisonneuve CB de, et al (2018) Crystal and melt inclusion timescales
967 reveal the evolution of magma migration before eruption. Nat Commun 9:2657. doi:
968 10.1038/s41467-018-05086-8

969 Schiano P, Monzier M, Eissen J-P, et al (2010) Simple mixing as the major control of the
970 evolution of volcanic suites in the Ecuadorian Andes. Contrib Mineral Petrol
971 160:297–312. doi: 10.1007/s00410-009-0478-2

972 Sheehan F, Barclay J (2016) Staged storage and magma convection at Ambrym volcano,
973 Vanuatu. J Volcanol Geotherm Res 322:144–157. doi:
974 10.1016/j.jvolgeores.2016.02.024

975 Shimizu K, Shimizu N, Komiya T, et al (2009) CO2-rich komatiitic melt inclusions in Cr-
976 spinels within beach sand from Gorgona Island, Colombia. Earth Planet Sci Lett
977 288:33–43. doi: 10.1016/j.epsl.2009.09.005

978 Shishkina TA, Botcharnikov RE, Holtz F, et al (2010) Solubility of H2O- and CO2-bearing
979 fluids in tholeiitic basalts at pressures up to 500 MPa. Chem Geol 277:115–125. doi:
980 10.1016/j.chemgeo.2010.07.014

981 Sorbadere F, Schiano P, Métrich N, Garaebiti E (2011) Insights into the origin of primitive
982 silica-undersaturated arc magmas of Aoba volcano (Vanuatu arc). Contrib Mineral
983 Petrol 162:995–1009. doi: 10.1007/s00410-011-0636-1

984 Steele-Macinnis M, Esposito R, Bodnar RJ (2011) Thermodynamic Model for the Effect of
985 Post-entrapment Crystallization on the H2O–CO2 Systematics of Vapor-saturated,
986 Silicate Melt Inclusions. J Petrol 52:2461–2482. doi: 10.1093/petrology/egr052

987 Sun S -s, McDonough WF (1989) Chemical and isotopic systematics of oceanic basalts:
988 implications for mantle composition and processes. Geol Soc Lond Spec Publ
989 42:313–345. doi: 10.1144/GSL.SP.1989.042.01.19

990 Toplis MJ (2005) The thermodynamics of iron and magnesium partitioning between olivine
991 and liquid: criteria for assessing and predicting equilibrium in natural and
992 experimental systems. Contrib Mineral Petrol 149:22–39. doi: 10.1007/s00410-004-
993 0629-4

994 Toramaru A, Noguchi S, Oyoshihara S, Tsune A (2008) MND(microlite number density)
995 water exsolution rate meter. J Volcanol Geotherm Res 175:156–167. doi:
996 10.1016/j.jvolgeores.2008.03.035

997 Wallace PJ, Kamenetsky VS, Cervantes P (2015) Melt inclusion CO_2 contents, pressures of
998 olivine crystallization, and the problem of shrinkage bubbles. Am Mineral 100:787–
999 794. doi: 10.2138/am-2015-5029

1000 Wang Z, Hiraga T, Kohlstedt DL (2004) Effect of H+ on Fe–Mg interdiffusion in olivine,
1001 (Fe,Mg)2SiO4. Appl Phys Lett 85:209–211. doi: 10.1063/1.1769593

1002 Warden AJ (1970) Evolution of Aoba caldera volcano, New Hebrides. Bull Volcanol 34:107–
1003 140. doi: 10.1007/BF02597781

1004 Wiart P (1995) Impact et gestion des risques volcaniques au Vanuatu. Notes Tech Sci Terre
1005 Geol-Géophysique N°13 Doc Trav ORSTOM 83

1006 Witham F, Blundy J, Kohn SC, et al (2012) SolEx: A model for mixed COHSCl-volatile
1007 solubilities and exsolved gas compositions in basalt. Comput Geosci 45:87–97. doi:
1008 10.1016/j.cageo.2011.09.021

1009 Yamamoto T, Nakamura Y, Glicken H (1999) Pyroclastic density current from the 1888
1010 phreatic eruption of Bandai volcano, NE Japan. J Volcanol Geotherm Res 90:191–
1011 207. doi: 10.1016/S0377-0273(99)00025-6

1012 Yang H-J, Kinzler RJ, Grove TL (1996) Experiments and models of anhydrous, basaltic
1013 olivine-plagioclase-augite saturated melts from 0.001 to 10 kbar. Contrib Mineral
1014 Petrol 124:1–18. doi: 10.1007/s004100050169

1015

ACKNOWLEDGEMENTS

This research was conducted following the 2017-2018 Ambae volcanic crisis. P.B. field assessment was funded by IRD. Y.M. acknowledges support from the CNRS (projet INSU-TelluS-SYSTER), National Geographic grant number CP-122R-17 (Trail by Fire II – Closing the Ring project) and from IRD. We thank Nordine Bouden and Etienne Deloule of CRPG (France) for their precious guidance during SIMS analysis. We thank Mhammed Benbakkar for ICP-AES analyses, Claire Fonquernie for help with sample preparation, and Jean-Marc Hénot for help with SEM and EBSD imaging. We thank Mike Jollands and anonymous referees for constructive and beneficial comments on the original manuscript.